Bachelor Thesis

Gamma-Ray Emission from Positron Annihilation inside the Local Bubble

Rudi Reinhardt

Würzburg, June 2023

Julius-Maximilians-Universität Würzburg
Faculty of Physics and Astronomy

Supervisor: Dr. Thomas Siegert

Abstract

Context: The characteristic gamma-ray line for positron annihilation appears at 511 keV. The 511 keV map of the Milky Way (INTEGRAL/SPI) might contain an isotropic contribution coming from positrons created inside the Local Bubble, that annihilate at the edges.
Aims: In this thesis we want to investigate whether the 511 keV signal coming from the Local Bubble contributes as foreground emission. Therefore, we calculate the expected gamma-ray line flux from positrons formed by the β^+ decay of ^{26}Al.
Methods: The fluxes are calculated using line of sight integration. Therefore, we describe the positron propagation inside and the diffusion in the shell of the Local Bubble. The positron density profile is estimated using simulation data for density and temperature structure of generic superbubbles. Assuming a quasi-steady state, we solve the differential equation of positron diffusion with simultaneous annihilation which is a rough estimate within the timescale between production and annihilation. Different assumptions lead to different estimates of the annihilation emmisivity. Four methods are derived, taking into account different timescales and models for positron propagation.
Results: Given the ^{26}Al yields, and semi-analytic form of density, temperature and annihilation rates, we find a flux of $4.9 \cdot 10^{-6} - 1.5 \cdot 10^{-5}\,\mathrm{ph\,cm^{-2}\,s^{-1}}$ with an isotropic fraction of 65%.
Conclusions: Simulations with the future COSI-SMEX instrument result in no significant detection of the expected Local Bubble emission compared to the Galactic background within its nominal mission time of two years.

Abstraktum

Kontext: Charakteristisch für die Annihilation von Positronen ist eine Photonenenergie von 511 keV. Das 511 keV Signal der Milchstraße (INTEGRAL/SPI) enthält möglicherweise einen isotropen Beitrag von Positronen, welche im Inneren der Lokalen Blase entstehen und an ihren Rändern annihilieren.
Ziele: Ziel dieser Thesis ist es, den Beitrag der 511 keV Emission der Lokalen Blase am Gesamtfluss unserer Galaxie abzuschätzen. Hierfür bestimmen wir den erwarteten Photonenfluss für Positronen, welche durch den β^+-Zerfall von ^{26}Al in der Lokalen Blase entstehen.
Methoden: Die entsprechenden Flüsse bestimmen wir durch eine Sichtlinienintegration. Wir bestimmen die Ausbreitung der Positronen im Inneren der Lokalen Blase, sowie deren Diffusion an ihren Rändern. Die Positronendichte zeigt ein bestimmtes Profil, welches wir mit Hilfe von Dichte und Temperatur einer Superbubble bestimmen. Die entsprechenden Daten stammen von Simulationen. Die Differenzialgleichung, welche die Diffusion der Postronen und deren gleichzeitig stattfindenden Annihilation beschreibt, lösen wir durch die Annahme eines quasi-stationären Zustandes. Dieses Verfahren bietet eine grobe Abschätzung unter Berücksichtigung der Zeitskalen zwischen Entstehung und Annihilation. Verschiedene Annahmen in Bezug auf die Ausbreitung der Positronen, sowie unter Berücksichtigung der zuvor genannten Zeitskalen, liefern uns vier verschiedene Methoden, um die Photonenemissivität abzuschätzen.
Resultate: Gegebene Parameter für Dichte, Temperatur und Annihilationsraten liefern uns Photonenflüsse im Bereich von $4.9 \cdot 10^{-6} - 1.5 \cdot 10^{-5}\,\mathrm{ph\,cm^{-2}\,s^{-1}}$. Der isotrope Anteil liegt hierbei bei 65%.
Schlussfolgerungen: Simulationen für die geplante COSI-SMEX Mission liefern kein signifikantes Ergebnis für die Emission der Lokalen Blase im Vergleich zum Hintergrund der Milchstraße.

Contents

1 Introduction

Even after 50 years of observation, the 511 keV signal from the center of the Milky Way is not fully understood yet. It originates from positron-electron annihilation, but we cannot explain the large amount of positrons today. The best-fit map of positron annihilation in the Milky Way is shown in Fig. 1 using data from INTEGRAL/SPI. One can see the bright bulge in the Galactic center, that outshines a thick disk. This can not bee seen in other wavelengths. However, if the disk and bulge are actually the Galactic disk and Galactic bulge is not entirely clear. This image might also contain a halo or an isotropic contribution, that current telescopes cannot observe. With the launch oft he Compton Spectrometer and Imager, COSI, in 2027, it might be possible to observe such an isotropic contribution, because is has a line sensitivity of $7.9 \cdot 10^{-6}\,\mathrm{ph\,cm^{-2}\,s^{-1}}$ for 511 keV photons [Tomsick and COSI Collaboration, 2022]. It functions as a Compton telescope so that it can observe isotropic emission.

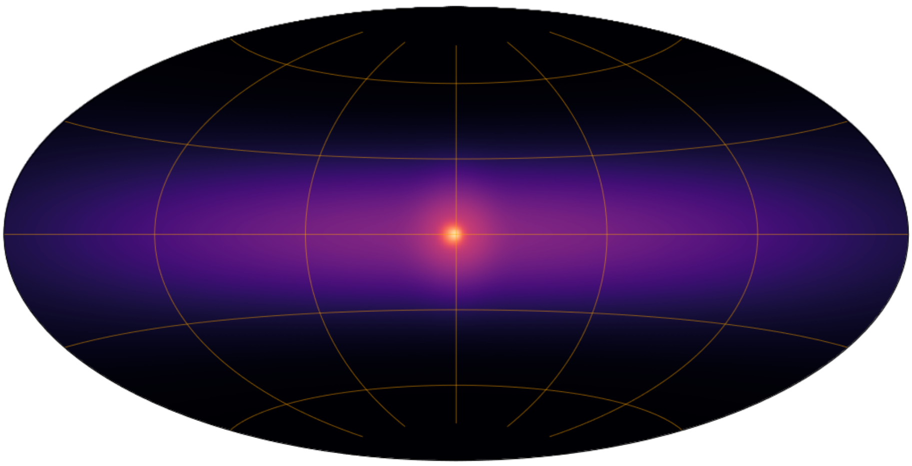

Fig. 1: Calculation of the sky as seen in the positron annihilation line at 511 keV. Figure taken from [Siegert, 2023].

One process as a source of positrons in our cosmic neighborhood is the β^+-decay of ^{26}Al produced by nucleosynthesis in massive stars. By stellar winds or as a result of a supernova they are finally spread into the interstellar medium (ISM). Our Sun is surrounded by an evacuated region of space with a temperature of $\sim 10^6$ K called the Local Bubble [Krause et al., 2014]. This superbubble was formed within the last $\sim 10^7$ years due to several supernovae within a small region of space and thus has a very low particle density ($\sim 10^{-3}\,\mathrm{cm^{-3}}$). Because of these supernovae, we would expect to find intermediate lifetime isotopes, such as ^{26}Al ($\tau_{26} = 1.03\,\mathrm{Myr}$) and ^{60}Fe ($\tau_{60} = 3.79\,\mathrm{Myr}$) also on Earth, and therefore also positron annihilation in our vicinity. The goal of this thesis is to understand the life cycle of these positrons inside a superbubble, starting from their formation inside the Local Bubble up to their annihilation in the outer regions. Based on a semi-analytical model for the flow of gas and positrons from inside out, we calculate the expected photon flux of positron annihilation in the Local Bubble. Predictions will be made regarding the significance of measuring this phenomenon with the COSI telescope. Further, distant superbubbles and their photon flux can also be simulated.

This thesis is structured as follows: in Chp. 2, the life cycle of positrons in the Milky Way is described. Chp. 3 outlines the physics of superbubbles and describes the Local Bubble in more detail. The propagation of positrons inside superbubbles and the application to the Local Bubble is explained in detail in Chp. 4. The expected gamma-ray line fluxes are modelled in Chp. 5. We simulate the expected flux for the design of the future COSI instrument in Chp. 6. Finally, we discuss our findings (Chp. 7) in the context of the literature and conclude in Chp. 8.

2 Life cycle of positrons in the Milky Way

In this chapter, the complete life cycle of positrons is described. After their formation the in-flight phase begins, in which different interactions with matter lead to energy losses. The last phase is the thermalization with the ISM, which results in the annihilation with electrons. This happens either directly or via positronium formation.The direct annihilation is also possible in flight. But given the much higher cross section for Positronium formation, this contribution is negligible and will be ignored in this thesis. The signature of electron-positron annihilation is the 511 keV line and the ortho-Positronium (oPs) spectrum below 511 keV. The line energy and cutoff energy of oPs spectrum corresponds to the rest mass of the particles, conserving energy, mass, momentum, charge, and spin.

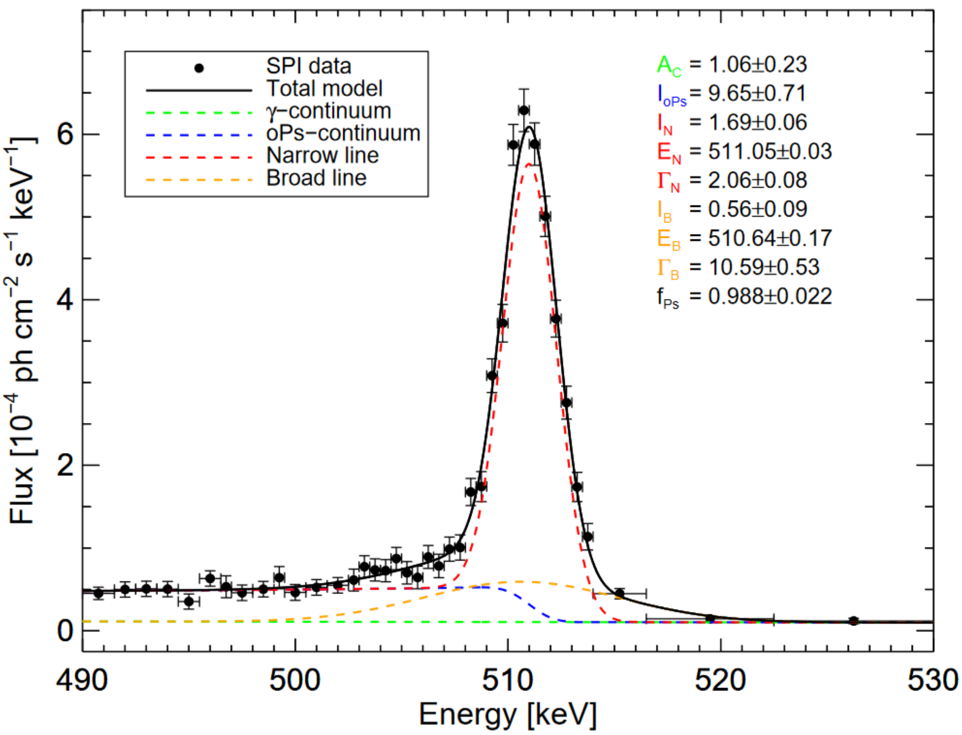

Fig. 2: Positron annihilation spectrum of the Galaxy. Shown are the SPI data points in black and four model components: narrow 511 keV line (red), broad 511 keV line (orange), ortho-positronium continuum (blue), Galatic -ray continuum (green). Figure taken from [Siegert et al., 2019].

2.1 Formation of positrons

Positrons are produced in our Galaxy by one of the following processes:

1. The β^+ decay of radioactive nuclei (e.g. ^{26}Al, ^{44}Ti or even ^{56}Ni)
2. Decay of π^+ into μ^+, which produces a positron
3. Photon-photon interactions, which decays itself into a positron
4. Pair production due to a photon interacting with a strong magnetic field

These processes are subject to the astrophysical environments: So we find the first process, the β^+ decay of radioactive nuclei, mainly in novae, supernovae or even Wolf-Rayet stars. The decay of π^+ into μ^+ and finally positrons is found in collisions of high energy cosmic rays ($\sim$ 200 MeV) with interstellar matter. The corresponding equations are the following:

$$\mathrm{p} + \mathrm{p} \rightarrow \mathrm{p} + \mathrm{p} + \pi^+ + \pi^-$$

$$\pi^+ \rightarrow \mu^+ + \nu_\mu$$

$$\mu^+ \rightarrow \mathrm{e}^+ + \bar{\nu}_\mu + \nu_\mathrm{e}$$

The third process (photon-photon interactions) $\gamma + \gamma \rightarrow \mathrm{e}^+ + \mathrm{e}^-$ requires high-energy photons (threshold energy 1.022 MeV) and thus takes place in the environment of compact objects, such as black holes, micro-quasars or active Galaxy nuclei (AGNs). The fourth and last process requires strong magnetic fields and is therefore found in the vicinity of (highly magnetized) neutron stars. In summary, the main sources of positron formation in our Galaxy are supernovae (SNe), novae, compact objects (neutron stars, black holes, etc.) and cosmic rays [Guessoum et al., 2005].

2.1.1 Radioactive decay of ^{26}Al

In the following, the β^+ decay of ^{26}Al will be discussed in more detail, since it is supposedly the main source of positrons in the Local Bubble.

The isotope ^{26}Al is produced in massive stars both hydrostatically (during H-burning) and explosively in the C-, Ne- or O-layers of the star. It is ejected either during strong stellar winds or during the explosion in a supernova. Current models provide yields of $\sim 10^{-4}$ $\mathrm{M}_\odot$ of ^{26}Al per star. This results in a production rate of 1.2-2.4 $\mathrm{M}_\odot$/Myr in our Galaxy by totaling over all stars [Siegert et al., 2023].
The isotope ^{26}Al has a half-life of $7.17 \cdot 10^5$ years. It decays to stable ^{26}Mg. In most cases (with a probability of 82%), it decays to an excited state of ^{26}Mg via β^+ decay, the remaining 18% is electron capture. After the deexcitation of ^{26}Mg, we obtain gamma-ray

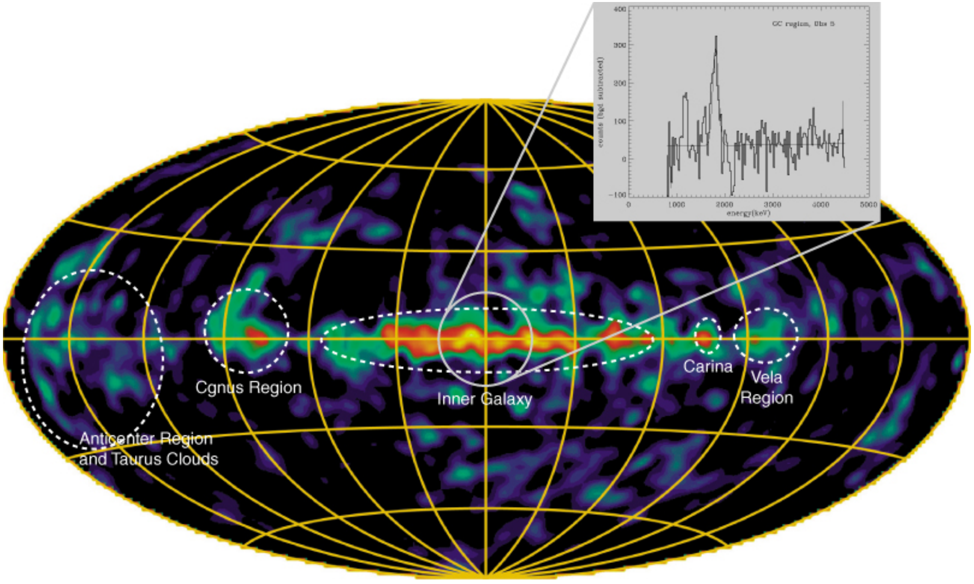

Fig. 3: The ^{26}Al distribution in the Milky Way. Shown is the 1.809 MeV gamma-ray line as measured with COMPTEL [Oberlack et al., 1996]. The bright spots represent concentrations of ^{26}Al in different massive star group as well as the Inner Galaxy. The spectrum from COMPTEL is shown in the inset. Figure taken from `https://heasarc.gsfc.nasa.gov/docs/cgro/cgro/comptel_al26.html`.

photons of 1809 keV [Diehl et al., 2021]. This deexcitation line provides direct evidence of ^{26}Al and is shown in Fig 3.
The decay equation looks the following:

$$^{26}\mathrm{Al} \rightarrow ^{26}\mathrm{Mg} + \mathrm{e}^{+} + \nu_{\mathrm{e}} \tag{1}$$

This radioactive decay of ^{26}Al is producing positrons with a probability of 82%. So that we would expect an annihilation flux of $2 \cdot 82\% = 164\%$ of the 1809 keV line. The 511 keV line would get about 20% of the total flux. So in a steady state configuration of ^{26}Al production, decay and final positron annihilation the 511 keV flux would be around 33% of the ^{26}Al flux. It can thus be a main source for annihilation emission in the Local Bubble. Positrons from the ^{26}Al decay follow a β^{+} decay (Fermi) spectrum, with a mean kinetic energy of 543.3 keV, up to an end point energy of 1.1 MeV. Thus, they are mildly relativistic with a Lorentz factor of up to ~ 3 [Prantzos et al., 2011].

2.2 In-flight phase

After the positrons are created, they propagate through the ISM. As charged leptons, they interact via the Coulomb force with other charged particles in their environment, namely: electrons, ions, atoms or molecules. Furthermore, they experience the electromagnetic and photon fields of the ISM. This results in a loss of energy and thus a deceleration of the positrons. The strength of the various interactions depends on the energy of the

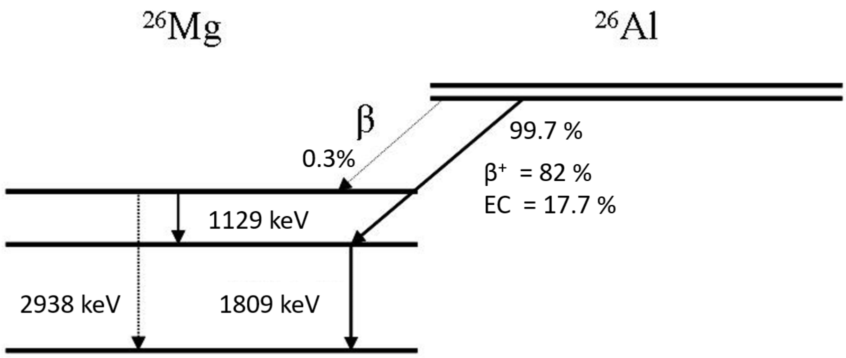

Fig. 4: Decay scheme of ^{26}Al. After decay into the excited state of ^{26}Mg, deexcitation occurs with emission of a 1809 keV photon. Probabilities and energies were added. EC means radioactive decay by electron capture. Figure taken from [Ohlendorf et al., 2010].

positrons, the density of the ambient gas and the strength of Magnetic fields. Fig. 5 shows the energy loss rate as a function of positron energy with the conditions of the warm ISM (T=8000 K).

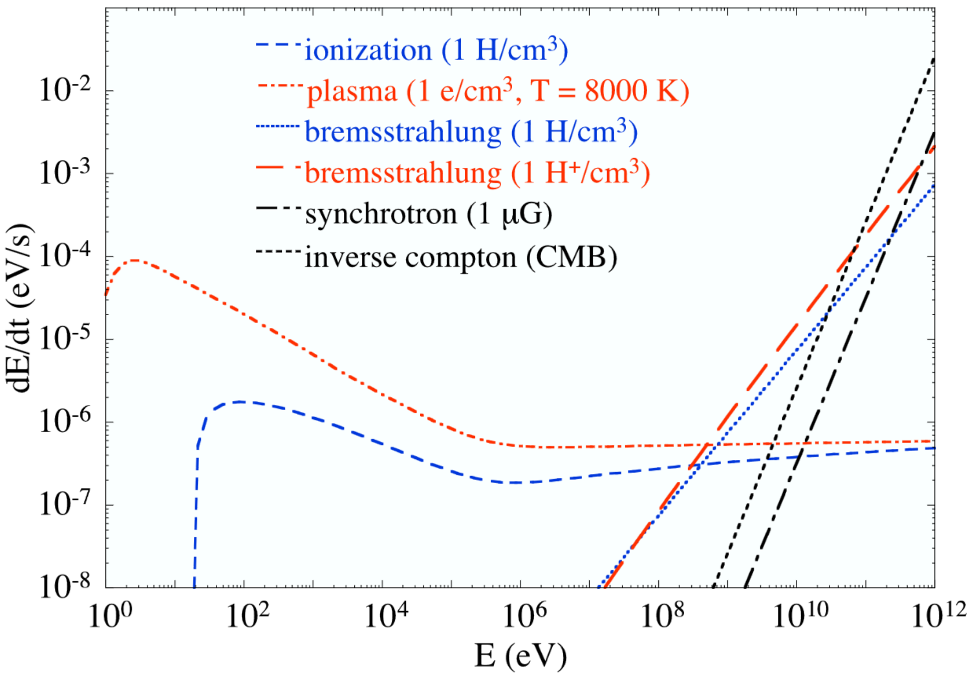

Fig. 5: Positron energy loss rate as a function of positron energy with the conditions of the ISM.You can see the different types of interactions and in which energy range they dominate. Figure taken from [Prantzos et al., 2011].

So as we can see, for our purposes (positrons with an initial maximum kinetic energy of 1.1 MeV) only plasma and ionisation losses are dominant. Inverse Compton (IC) and Synchrotron radiation (SYN) are negligible. Bremsstrahlung scales with the density of the gas like ionisation and is still ~ 3 orders of magnitude smaller than ionisation losses. Therefore, for our model, we only include plasma and ionisation losses. In the following we will describe these in more detail.

Plasma losses occur mainly via Coulomb scatterings with free electrons or inelastic interactions with atoms and molecules. The consequence is a continuous energy loss of the positrons. The different inelastic reactions produced by positrons and their energy threshold are shown in 1.

The energy loss rate of positrons in a cold plasma such as in the various phases of the ISM was described by [Prantzos et al., 2011]:

$$\left(\frac{\mathrm{dE}}{\mathrm{dt}}\right)_{\mathrm{COU}} = -7.7 \cdot 10^{-9}\ \frac{\mathrm{n_e}}{\beta}\ \left[\ln\left(\frac{\gamma}{\mathrm{n_e}}\right) + 73.6\right]\mathrm{eV/s} \tag{2}$$

Here $\mathrm{n_e}$ is the electron density of the ISM in cm^{-3}, $\beta = (\frac{v}{c})$ and $\gamma = \sqrt{\frac{1}{1-\beta^2}}$.

The inelastic collisions of positrons with molecules and atoms can be considered as a continous process over the timescale of propagation. The energy loss can be determined by the Bethe-Bloch formula. The ionisation losses are larger than the excitation losses. An approximation of this process is also given by [Prantzos et al., 2011]:

$$\left(\frac{\mathrm{dE}}{\mathrm{dt}}\right)_{\mathrm{ION}} = -7.7 \cdot 10^{-9}\ \frac{\mathrm{n} \cdot \mathrm{Z}}{\beta}\ \left[\ln\left(\frac{(\gamma-1)(\gamma\beta \mathrm{m_e c^2})^2}{2\mathrm{I}^2}\right) + 0.125\right]\mathrm{eV/s} \tag{3}$$

Where n is the neutral atom density in cm^{-3}, Z is the electron number of the atom (one for hydrogen) and I is the ionization potential (13.6 eV for hydrogen). We can calculate the range of the positrons losing energy due to ionisation and plasma losses combined by

$$\mathrm{R} = \int_{\mathrm{E_{in}}}^{0} \frac{\mathrm{dE}}{\left|\frac{\mathrm{dE}}{\mathrm{dt}}\right|} \cdot \frac{\mathrm{dr}}{\mathrm{dt}} = \int_{\mathrm{E_{in}}}^{0} \frac{\mathrm{dE}}{\left|\frac{\mathrm{dE}}{\mathrm{dt}}\right|} \cdot \mathrm{v(E)}$$

where

$$\left(\frac{\mathrm{dE}}{\mathrm{dt}}\right) = \left(\frac{\mathrm{dE}}{\mathrm{dt}}\right)_{\mathrm{ION}} + \left(\frac{\mathrm{dE}}{\mathrm{dt}}\right)_{\mathrm{COU}}$$

We estimate ranges of $\sim 400 - 600$ pc depending on the radius of the Local Bubble (larger radius means higher range cause the positrons hit the high density shell later). Thus the positrons will not annihilate inside the Local Bubble. There are also a few positrons which annihilate or form positronium in-flight. These processes are not discussed in detail. We only consider annihilations of cooled positrons.

Process	Threshold (eV)
$e^+ + H \rightarrow Ps + H^+$	6.8
$e^+ + H \rightarrow e^+ + e^- + H^+$	13.6
$e^+ + H \rightarrow e^+ + H^*$	10.2
$e^+ + H \rightarrow e^+ + H^{**}$	12.1
$e^+ + He \rightarrow Ps + He^+$	17.8
$e^+ + He \rightarrow e^+ + e^- + He^+$	24.6
$e^+ + He \rightarrow e^+ + He^*$	21.2
$e^+ + H_2 \rightarrow Ps + H_2^+$	8.6
$e^+ + H_2 \rightarrow e^+ + e^- + H_2^+$	15.4
$e^+ + H_2 \rightarrow e^+ + H_2^*$	12.0

Tab. 1: Reactions of positrons with the ISM and their energy thresholds. The table was taken from [Guessoum et al., 2005].

2.3 Thermalisation and annihilation processes

Once the positrons have reached the energies of the ambient environment, they are "thermalized" with the gas. This means that their energy distribution relaxes to a Maxwellian distribution with the temperature of the interstellar gas. The positrons undergo a number of different processes that finally lead to their annihilation, either directly or via positronium formation. The positron reaction rates of those processes are shown in Fig. 6. For later purposes, three of these processes will now be discussed in more detail.

2.3.1 Charge exchange with H

Positrons interact with an electron from a hydrogen atom in their ambient medium to form positronium. In Fig. 6, it can be seen that in the range between $\sim (10^4 - 10^6)$ K, the charge exchange shows the largest interaction cross-section and thus provides the highest annihilation rates. At temperatures below the energy threshold of 6.8 eV (Tab. 1) charge exchange is excluded and may only happen in the tail of the Maxwellian distribution. In general, this will be very rare in the cold ISM ($T_{dust} \sim 100$K and $T_{gas} \sim 10$K). It can also not happen in the hot phases of the ISM, where the hydrogen is completely ionized. This explains the cut-off of the annihilation rate at about $5 \cdot 10^6$ K.

2.3.2 Radiative recombination with free electrons

In this process, a positron interacts with a free electron and also forms positronium. The cross section is larger than for charge exchange at temperatures below $\sim 10^4$ K. For this reason radiative recombination is relevant for low temperatures if enough free electrons are available.

2.3.3 Direct annihilation with free electrons

Here, positrons annihilate directly with electrons of the ISM, without the formation of positronium. The cross section is only above that of radiative recombination for temperatures higher than $\sim 10^6$ K.

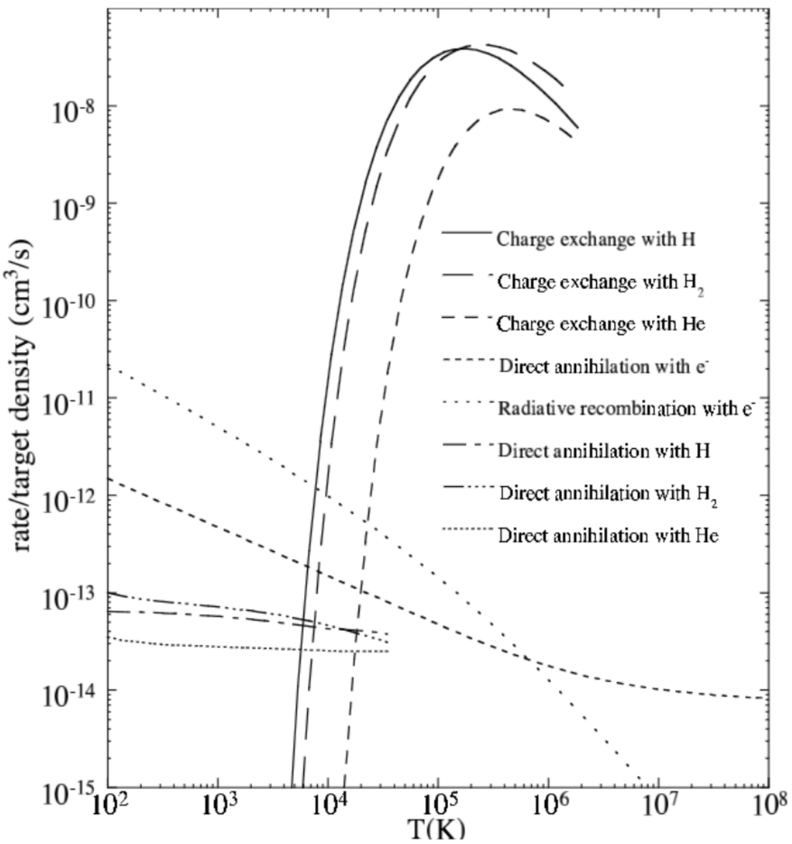

Fig. 6: Positron reaction rates as a function of positron temperature [Guessoum et al., 2005].

As a summary of all previously mentioned, Fig. 7 shows an overview of the positron life in the ISM:

After their formation (top), the positrons lose energy due to the above-mentioned processes of ionisation and plasma scattering. While only a small fraction annihilates in flight, the majority will cool enough and thermalise with the ISM. the dominant annihilation reactions are then charge exchange (only possible above 6.8 eV), and radiative reombination with free electrons. These processes occur via positronium formation.

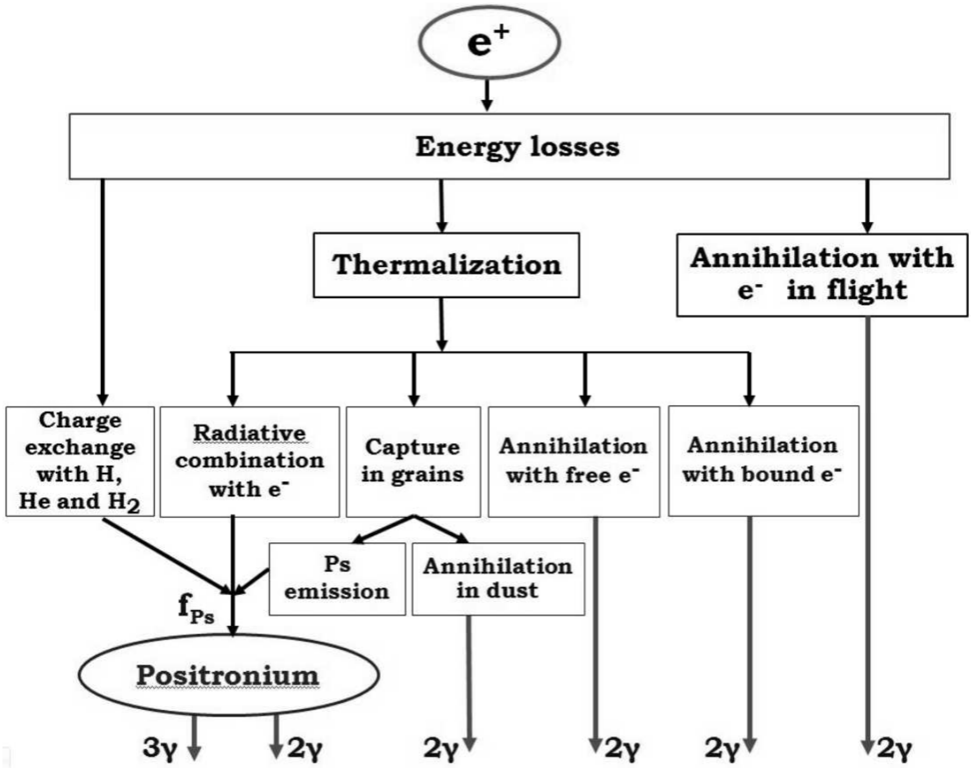

Fig. 7: Scheme of the positron life cycle. It contains energy losses, thermalisation and the different annihilation processes as discussed before [Prantzos et al., 2011].

2.3.4 Positronium formation

Positronium (Ps) is a bound state of a positron with an electron. As mentioned before, it is formed during both charge exchange and radiative recombination and thus plays an important role in the annihilation process. The state of Ps can be treated as the one of hydrogen atom. Depending on the relative orientations of the spins of the positron and the electron, the Ps ground state has two possible spin states. There is a singlet state with antiparallel spins (total spin $S_{tot} = 0$) called para-positronium (pPs). The triplet state for which positron and electron have parallel spins ($S_{tot} = 1$) is known as ortho-positronium (oPs). Following from the (2S+1) spin degeneracy, the pPs state will be formed in 1/4 of the time and the oPs state will be formed in 3/4 of the time. The lifetimes of the different states before annihilation (in vacuum) are $1.2 \cdot 10^{-10}$ s for pPs and $1.4 \cdot 10^{-7}$ s for oPs. The release of annihilation photons is constrained by conservation of momentum and spin. The pPs releases two photons of 511 keV (as in the case of direct annihilation). The oPs, on the other hand, is forced by spin conservation to create an odd number of photons with a total energy of 1022 keV (due to momentum conservation) producing a continuum of energies up to 511 keV [Prantzos et al., 2011]. For the majority of cases, three photons are created. Fig. 8 shows the oPs annihilation spectrum. One can see the peak (which is also the cut-off) at 511 keV. The number of photons created decreases for lower energies. The pPs spectrum on the other hand looks like the spectrum of direct annihilation, due to the creation of two 511 keV photons. It can bee seen as the peak in Fig. 2.

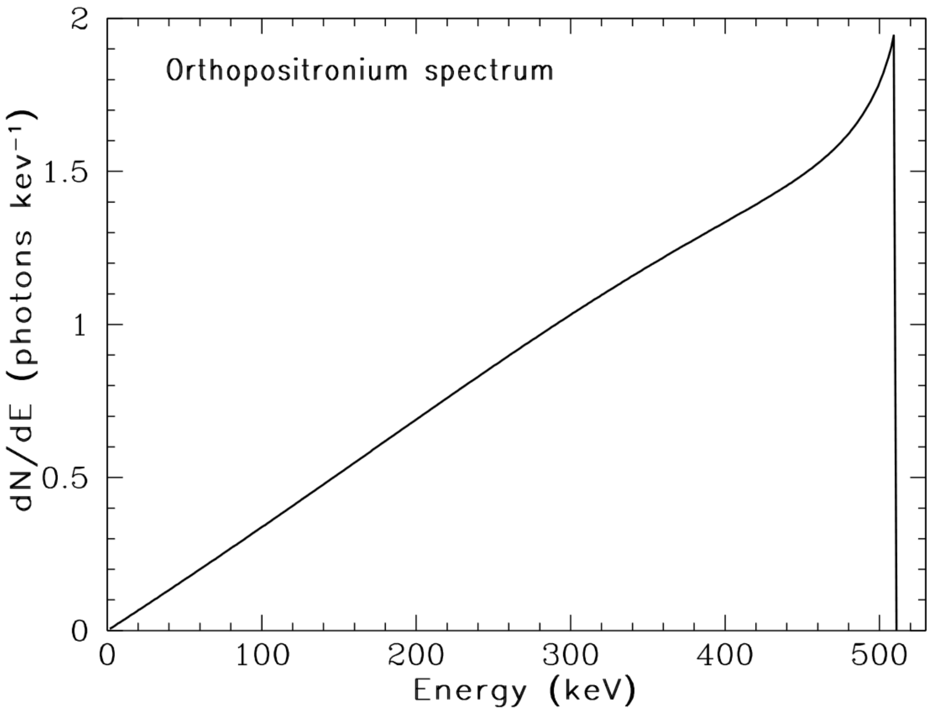

Fig. 8: Three photon spectrum of ortho-positronium annihilation. Figure taken from [Prantzos et al., 2011].

3 The Local Bubble

3.1 Superbubbles

Superbubbles belong to the elementary components of the Galactic ISM. They are structures of low particle density ($\sim 10^{-3}\,\mathrm{cm}^{-3}$) but high temperatures ($\sim 10^{6}\,\mathrm{K}$), which are surrounded by a region of higher density of atoms like hydrogen, as well as some dust which can be used to estimate the boundaries in the case of the Local Bubble [Pelgrims et al., 2020]. They have typical sizes of a few 100 pc. The expansion of these superbubbles is driven by the energy output of massive stars and supernovae (SNe). Ideally, it is determined just by the energy injection from stellar winds and SNe, as well as the density of the surrounding ISM. At the edges, however, their expansion is influenced by adjacent bubbles. Together, these phenomena determine the morphology of a superbubble. The compression of matter at the edges of such a cavity leads to the formation of new stars. Their evolution is given by three phases. The first phase is characterized by an expansion in an adiabatic flow. Here, the system can not be cooled with radiation, cause this process is too slow compared to the rapid expansion. Surrounding gas is swept up by this flow. This results in a thin shell of interstellar gas emerging in the second phase. Finally, the expansion of the outer regions is slowed down due to radiative cooling which becomes more effective in the third and last phase of the superbubble evolution [Pleintinger, 2020]. Fig. 9 schematically shows this whole process of superbubble evolution.

3.2 The Bubble surrounding the Solar System

The Local Bubble as our "home" superbubble was entered by the Sun about 5 Myr ago. Today our Solar System is located in its central region. This is shown in Fig. 10 by simulations of [Zucker et al., 2022][1].

As previously mentioned, the formation of superbubbles is initiated by the energy output of massive star winds and SNe. The origin of the Local Bubble is about 14 Myr ago. It be related to SNe in Upper Centaurus Lupus (UCL) and Lower Centaurus Crux (LCC). Subsequently the expansion was driven forward by further momentum injections due to additional SNe (estimations suggest about 15). At the same time, the Local Bubble is

[1] https://faun.rc.fas.harvard.edu/czucker/Paper_Figures/Interactive_Figure1.html

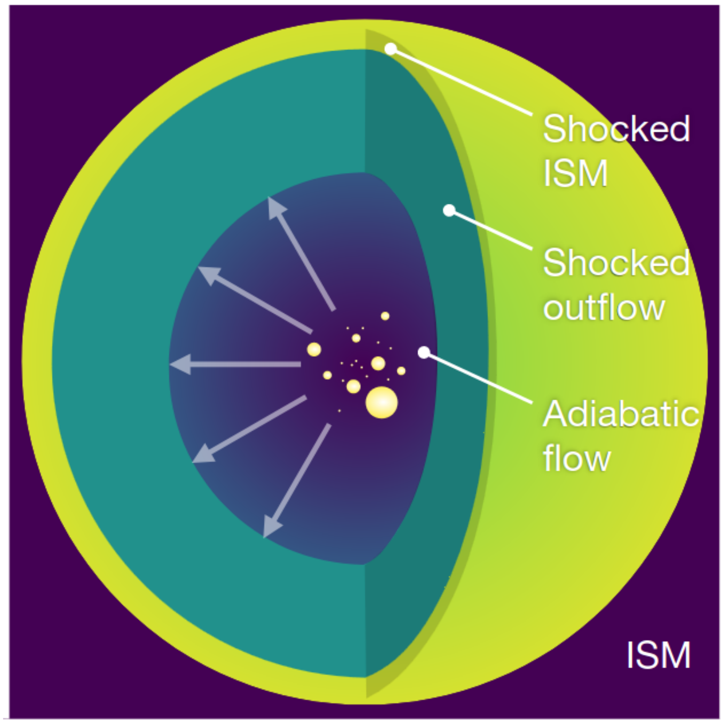

Fig. 9: Schematic structure of a superbubble. Scheme taken from [Pleintinger, 2020]

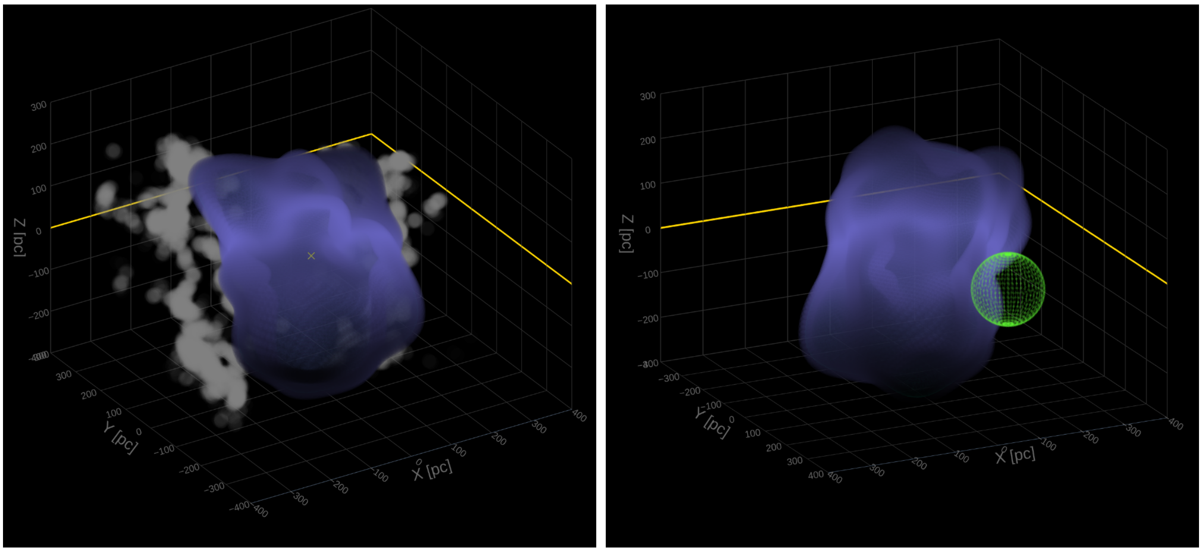

Fig. 10: Left: Model of the Local Bubble with the Sun (yellow cross) in the central region. We can see the dust (gray) surrounding the shell. Right: The expansion of the Local Bubble is constrained by the adjacent Per Tau Bubble. Pictures were taken from a simulation of [Zucker et al., 2022].

confined at its edges. For example, the neighboring Per Tau Bubble limits the expansion (Fig. 10). Together, these processes result in the present "potato-like" shape of the Local Bubble. Its extent is between 100 to 300 pc from the Solar System. This can be seen on the left side of the Fig. 10. Also noticeable here are the dust clouds surrounding the edges of the Local Bubble. From these arise several star forming regions, like Lupus, Ophiuchus or Corona Australis [Zucker et al., 2022]. This is shown in Fig. 11[2].

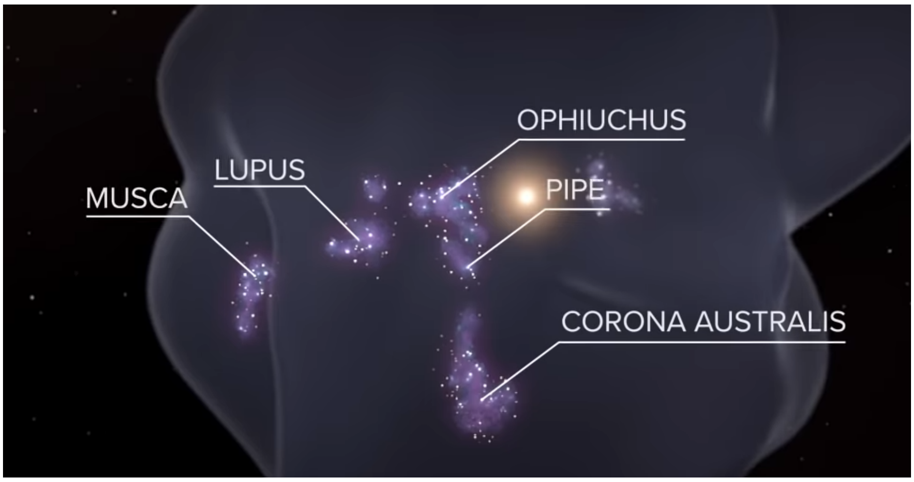

Fig. 11: Star forming regions at the edges of the Local Bubble. This Picture was taken from [Zucker et al., 2022].

[Zucker et al., 2022] have also performed a simulation showing the entire evolution of the Local Bubble since its formation 14 Myr ago (top left of Fig. 12). It shows the motion of the Sun around the Galactic center into the bubble (bottom left). Selected times from 14, 10 and 5 Myr ago as well as the present constellation are shown in Fig. 12. It becomes evident that the amorphous structure of the Local Bubble today has only formed within the last 5 Myr (compare bottom left with bottom right).

3.2.1 Modelling the structure of the Local Bubble

For further purposes of this thesis it will be necessary to model the structure of the Local Bubble. To obtain usable data, [Zucker et al., 2022] made use of measurements of dust extinctions. This method is convenient because the dust is located at the edges of the Local Bubble. [Zucker et al., 2022] provide expansions of their dust extinction data into spherical harmonics. We investigated different maximum multipole levels and describe these levels by a complexity parameter i. The bubble is spherical with the Sun near but not at its center for a multipole level of $i = 0$. Low orders ($i=1$ or 2) provide structures that are not complex enough. Many data points are not represented adequately. For very high orders ($i > 5$), on the other hand, the shape looks partially discontinuous and also unphysical. The best result appears to be around $i = 3$ or 4. We will use $i=3$ as a compromise between complexity and predictiveness of the Local Bubble shape. In Fig. 13, the radii as a function of Galactic coordinates are illustrated, indicating the variation for $i=1$ (130 to 290 pc), up to $i = 8$ (80 to 360 pc). These different orders of expansion can provide some sort of systematic uncertainty in the resulting fluxes.

[2] `https://www.cfa.harvard.edu/news/`

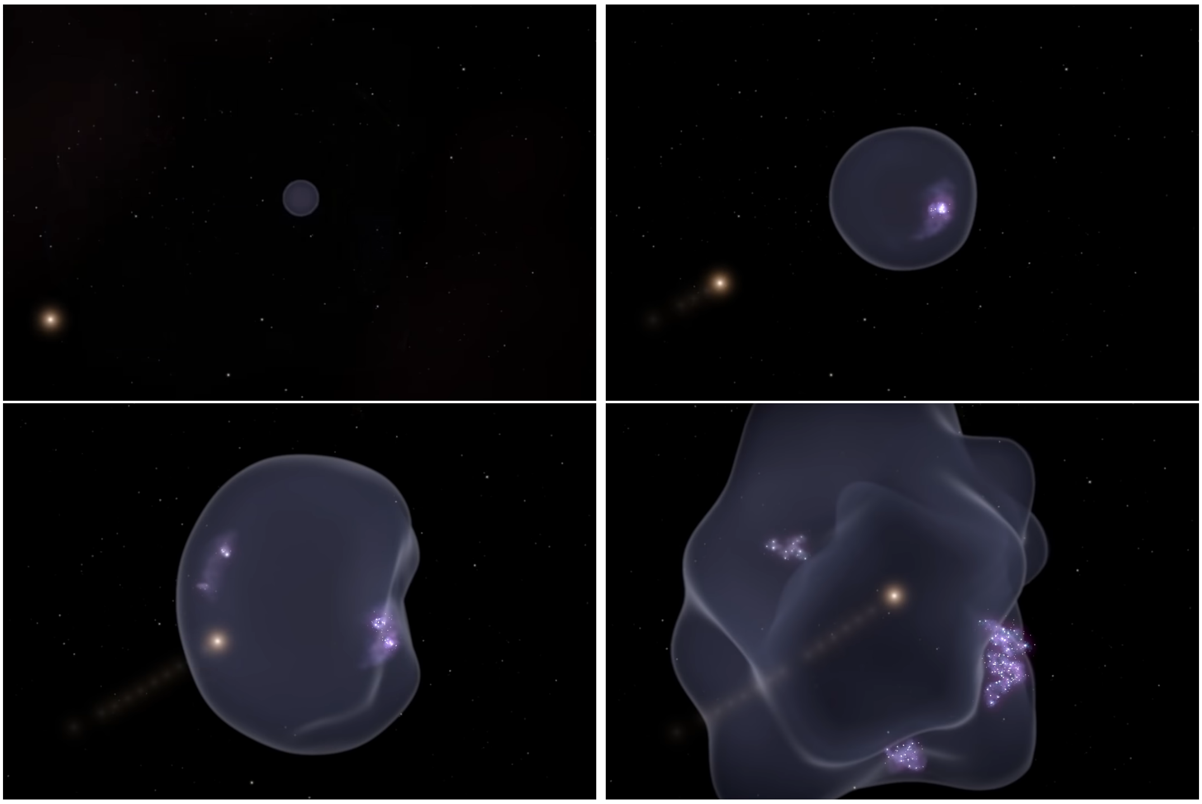

Fig. 12: Simulation by [Zucker et al., 2022] showing the evolution of the Local Bubble.
Top left: Formation out of SNe with the Sun several 100 pc away (14 Myrs ago)
Top right: Local Bubble and the Sun 10 Myrs ago
Bottom left: The Sun enters the Local Bubble (5 Myrs ago)
Bottom right: Todays Situation with the Sun in the center.

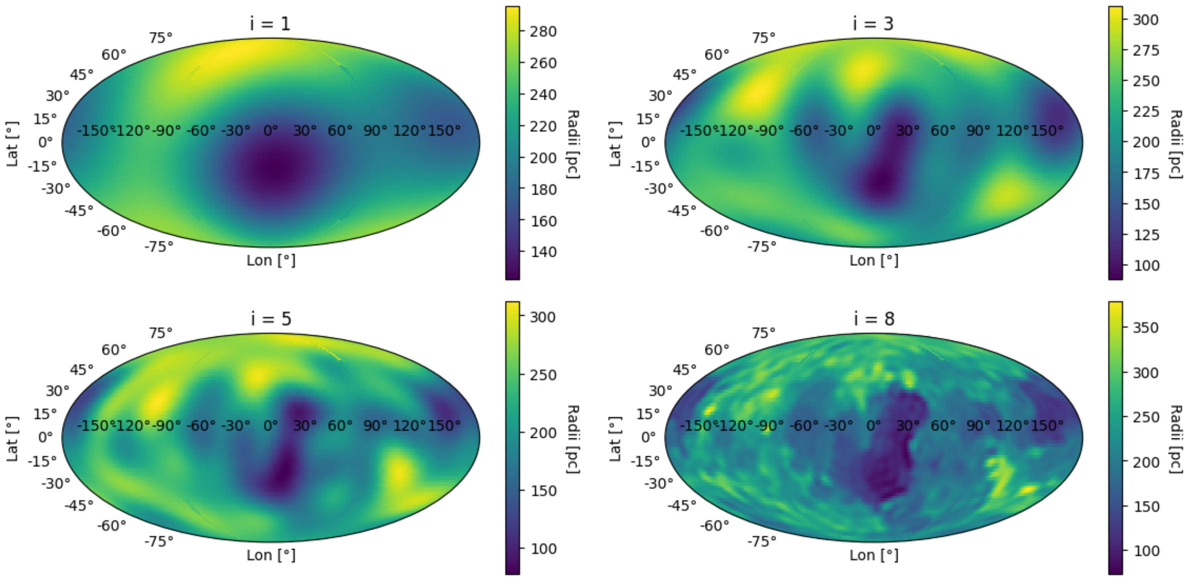

Fig. 13: Different calculations $\left[\mathrm{i} = 1(\text{Top left});\ 3(\text{Top right});\ 5(\text{Bottom left});\ 8(\text{Bottom right})\right]$ for modelling the shape of the Local Bubble.

3.2.2 Assumed properties of the Local Bubble

Later, we want to calculate the propagation of positrons through the Local Bubble (Chp. 4). It would be preferential to have independent measurements of the particle density and temperature inside the bubble. Cause such data are not available, we use the simulations by [Krause et al., 2014] for a canonical superbubble with 3 SNe and a total energy input of 10^{51} erg for our model assumptions. In the inner regions we have a particle density in the order of $\sim\ 10^{-27}\,\mathrm{g/cm^3}$ due to the simulations, while in the outer regions it is around $\sim\ 10^{-23}\,\mathrm{g/cm^3}$. The resulting density profile from the hydrostatic simulations is shown in Fig. 14. It can be seen that the profile can be approximated by a Fermi distribution very well within orders of magnitude (see later Chp. 4). The same applies to the temperature distribution of the plasma, which we can also obtain from the simulations. While it is approx. $\sim 5 \cdot 10^6\,\mathrm{K}$ in the inner regions, it is only about $\sim\ 10^2\,\mathrm{K}$ outside the shell, according to the Saha equation.

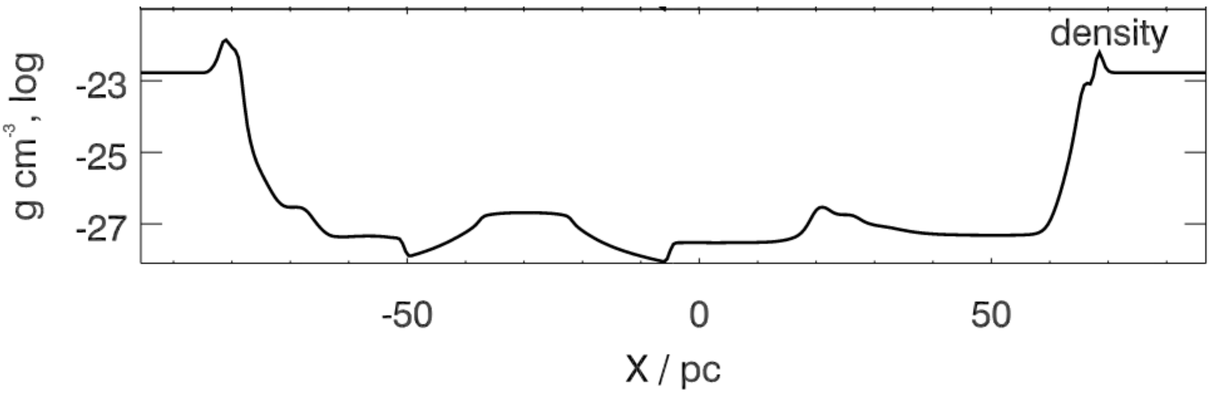

Fig. 14: The particle density of a superbubble due to computer simulations [Krause et al., 2014].

4 Propagation of positrons in the Local Bubble

In this chapter we will make use of the previous findings to describe the propagation of positrons within the Local Bubble. Here we first look at the energy loss of the particles, in order to determine the annihilation rates as a function of the radius. This depends on the positron temperature, i.e. energy, as can be seen in Fig. 6.

4.1 Energy loss and temperature

4.1.1 Density and energy loss rates

The positrons are created with a mean energy of 543.3 keV [Prantzos et al., 2011] from ^{26}Al decay, which we use as canonical injection energy in the following. To calculate their energy loss inside the Local Bubble, we make use of equations 2 and 3. These equations describe plasma and ionization losses and dominate in this energy range (Fig. 5). We also make the assumption that only hydrogen is ionized. Thus, the complete energy loss depends only on the particle density and the positron energy. We thus take the data from Fig. 14 and describe them with a Fermi function (Fig. 15). Then the function is adapted to the edges of the Local Bubble (here $r_0 = 150\,\mathrm{pc}$, since this is the average radius).

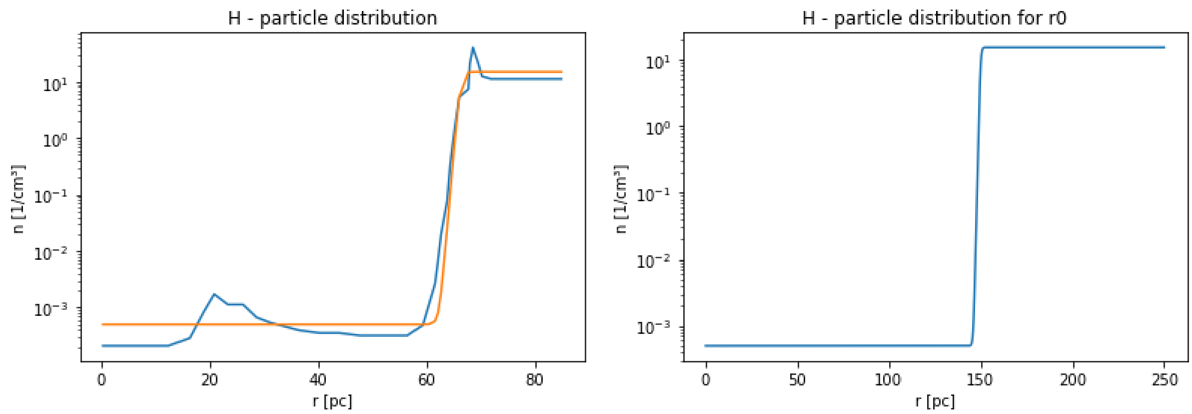

Fig. 15: Left: The particle density with data from the simulations of [Krause et al., 2014] (blue) fitted with the function of equation 4(orange).
Right: The fit function stretched to a radius of 150 pc.

$$n_H = a + b \cdot \frac{1}{1 + \exp\left(-\frac{r - r_0}{d}\right)} \tag{4}$$

Fig: 15 shows the simulated data from [Krause et al., 2014] on the left side fitted with the Fermi function according to equation 4, where a is the particle density inside and b the density outside the bubble. r_0 is the radius of the bubble and d is the range over which the density increases. We obtain the following fit parameters: $a = 0.51 \cdot 10^{-4}\mathrm{cm}^{-3}$, b = 15.09 cm^{-3}, r_0 = 66.1 pc, d = 0.38 pc. In the right plot of Fig.15 is the fitted Fermi function for a bubble radius of 150 pc. Therefore the parameter d is strechted by the ratio of the two radii $(\frac{150\,\mathrm{pc}}{66.1\,\mathrm{pc}})$. The initial energy of 543.3 keV corresponds to values of $\gamma = 2.06$ and $\beta = 0.87$. If we insert these values together with n_H into the energy loss equations (2 and 3), we get the energy loss as a function of time. To obtain a rough estimate of the energy loss per parsec, we assume that the transport will always go from smaller to larger radii (inside out). The energy losses are only important at larger radii. For these assumptions the loss per distance is:

$$\frac{dE}{dr} = \frac{dE}{dt} \cdot \frac{dt}{dr} = \frac{dE}{dt} \cdot \frac{1}{v} \tag{5}$$

After carrying out the above steps, the following energy loss rates are obtained:

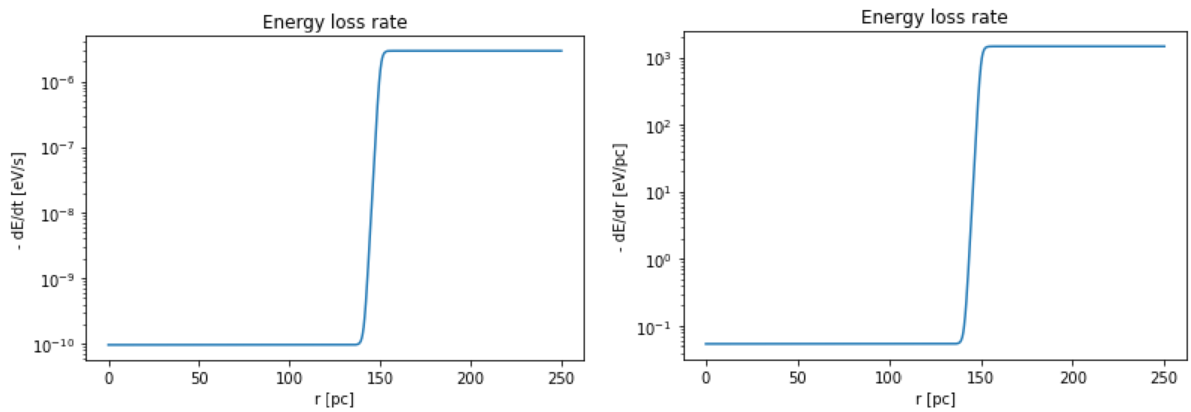

Fig. 16: Energy loss rate per time $-\frac{dE}{dt}$ (left) and per distance $-\frac{dE}{dr}$ (right)in the Local Bubble.

It can be seen that the energy loss, similar to the density, also follows a Fermi distribution. This is expected since plasma and ionization losses are both linear in particle density. This leads to the fact that the positrons in the interior lose only very little of their energy. However, when they finally reach the edges, with their high hydrogen density, the energy loss increases by several orders of magnitude. The conclusion and prediction is therefore an abrupt deceleration of the positrons at the edges of the Local Bubble.

4.1.2 Determination of the positron energy function

The process of positron propagation will be simulated as follows: We use a step size of $\Delta r = 1\,\mathrm{pc}$ to calculate the new energy due to energy losses as $E_{i+1} = E_i - dE/dr \cdot \Delta r$. Here, dE/dr is the energy loss rate per distance, E_i is the energy of the previous step. In each step, the particle velocity, v, and correspondingly β and γ are updated. However, it is to be noted that the positrons do not move outwards in a direct, i.e. ballistic, way. Rather, they perform a "random walk". Due to the scattering pitch angle in the turbulent magnetic fields and also Coulomb interactions with other particles, the positrons are scattered several times. To account for this phenomenon, we describe the net outward motion as a diffusion process. The characteristic length scale L of such a process is given by:

$$L = \frac{D}{2 \cdot v} \tag{6}$$

v is the positron velocity and D is the diffusion coefficient. We keep the diffusion coefficient as a free parameter cause it is unknown for our case of low-energy positrons in a thin or dense gas. Typical values for high-energy particles in the ISM are about $10^{27}\,\mathrm{cm^2\,s^{-1}}$, so that we will probe a range of 10^{22}–$10^{32}\,\mathrm{cm^2\,s^{-1}}$ to cover the full range of possibilities. In the calculations we set $D = 10^{30}\,\mathrm{cm^2\,s^{-1}}$. The diffusion coefficient will also play an important role in determining the range within which the positrons annihilate.

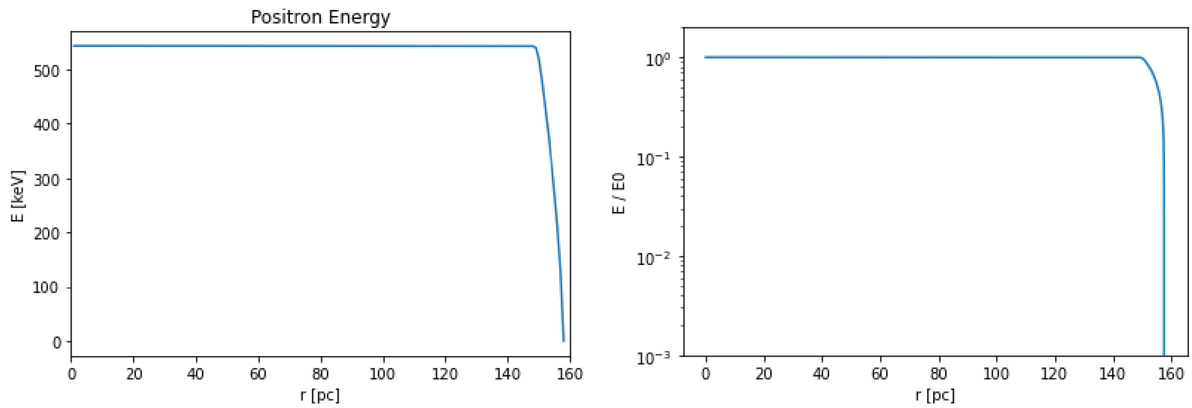

Fig. 17: Left: Estimated positron energy distribution for the case of the density profile shown in Fig. 15.
Right: Energy distribution in relation to the initial energy E/E_0

As expected from the thin gas inside the bubble, the energy lost inside is negligible. At the edge, however, the positron energy decreases abruptly. Also this curve can be approximated by a Fermi function with a zero offset.

$$E_{kin} = E_0 \cdot \frac{1}{1 + \exp(\frac{r - r_T}{f})} \tag{7}$$

E_0 is the initial energy and r_T is the radius where the positrons have lost half their energy.

f is range over which the energy decreases.

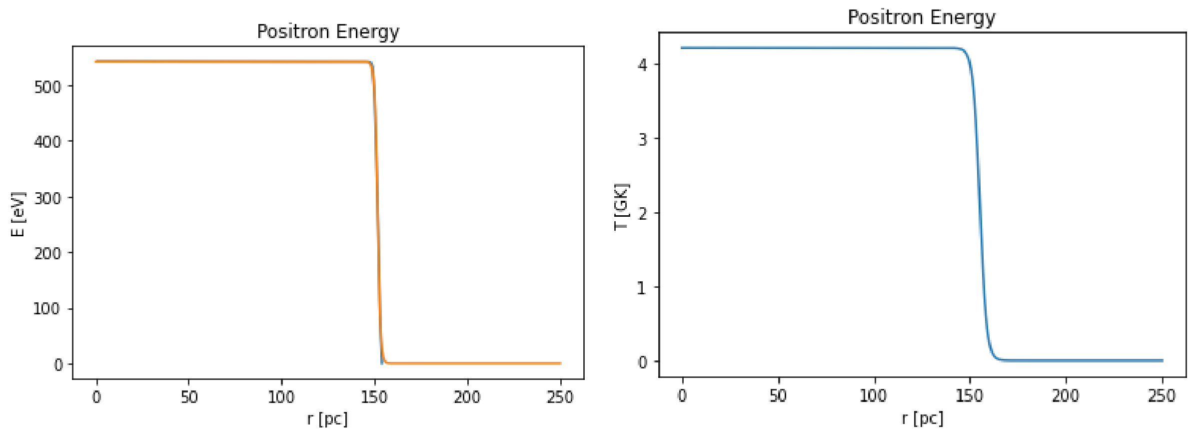

Fig. 18: Energy (left) and corresponding temperature distribution (right) of positrons in the Local Bubble.

Fig. 18 shows the energy distribution of the positrons within the Local Bubble. The fitting parameters are the following: E_0 = 543.3 keV, r_0 = 154.75 pc, f = 1.71 pc. In addition, the values were converted into a temperature curve using the equation:

$$\mathrm{T} = \frac{2}{3} \cdot \frac{\mathrm{E_{kin}}}{\mathrm{k_B}}$$

Where $\mathrm{k_B}$ is the Boltzmann constant with a value of $1.38 \cdot 10^{-23}\,\frac{\mathrm{J}}{\mathrm{K}}$.

4.2 Diffusion and Annihilation

In order to describe the density profile of *annihilating* positrons, $\mathrm{n}^*(\mathrm{r})$, as they propagate diffusively, we define the change of the density with time as the linear combination of a diffusion term, A(r), and an annihilation term, B(r):

$$\frac{\mathrm{d\,n}^*}{\mathrm{dt}} = \mathrm{A(r)} + \mathrm{B(r)} \tag{8}$$

Here, we describe the density as a function of radius r, i.e. we approximate the situation in one dimension, even though the Local Bubble has an asymmetric shape. For the angle dependence, we would need to model the shear and mixing, which is also unknown. Therefore, we simplify the model and apply the result towards each direction of the Local Bubble. The diffusion term,

$$\mathrm{A(r)} = 4\pi \cdot \mathrm{v}\left[\mathrm{n}^*(\mathrm{r}) \cdot \mathrm{r}^2 - \mathrm{n}^*(\mathrm{r} + \mathrm{dr}) \cdot (\mathrm{r} + \mathrm{dr})^2\right]$$

describes the flow of particles with velocity v within a shell of $[r, r + dr]$.

The annihilation term,

$$\mathrm{B(r)} \;=\; -\,4\pi \mathrm{r}^2 \cdot \mathrm{a(T)\,n^*(r)\,n_H(r)\,dr}$$

describes the change of the positron density due to annihilation within the volume $\int 4\pi^2\,\mathrm{dr}$. Here, $\mathrm{n_H(r)}$ is the particle density in the Local Bubble according to Fig. 15, a(T) are the annihilation rates corresponding to positron temperature according to Fig. 6.
For an observer time scale, the process can be approximated by a steady state:

$$\frac{\mathrm{d\,n^*}}{\mathrm{dt}} \stackrel{!}{=} 0$$

Since the particles are moving diffusively, we replace the velocity with the diffusion coefficient at the radius r.

$$\mathrm{v} \;=\; \frac{\mathrm{D}}{2 \cdot \mathrm{r}}$$

The final differential equation then reads:

$$0 \;=\; 2\pi \mathrm{D}\big[\mathrm{r\,n^*(r)} \;-\; \mathrm{r\,n^*(r\,+\,dr)} \;-\; \mathrm{dr\,n^*(r\,+\,dr)}\big] \;-\; 4\pi \mathrm{r}^2 \cdot \mathrm{a(T)\,n^*(r)\,n_H(r)\,dr}$$

Next, we make use of the definition of a derivative and can see that:

$$\big[\mathrm{r\,n^*(r)} \;-\; \mathrm{r\,n^*(r\,+\,dr)}\big] \;=\; -\,\mathrm{r} \cdot \frac{\delta \mathrm{n}^*}{\delta \mathrm{r}}\,\mathrm{dr}$$

After this transformation we divide the whole differential equation by $2\pi\,\mathrm{D\,r\,dr}$ and get:

$$0 \;=\; -\,\frac{\mathrm{d\,n^*}}{\mathrm{dr}} \;-\; \frac{\mathrm{n^*(r\,+\,dr)}}{\mathrm{r}} \;-\; 2 \cdot \mathrm{a(T)\,n^*(r)\,n_H(r)} \cdot \frac{\mathrm{r}}{\mathrm{D}}$$

After this step, it is convenient to preform the limit $\mathrm{dr} \to 0$

$$0 \;=\; \lim_{\mathrm{dr}\to 0}\left(-\,\frac{\mathrm{d\,n^*}}{\mathrm{dr}} \;-\; \frac{\mathrm{n^*(r\,+\,dr)}}{\mathrm{r}} \;-\; 2 \cdot \mathrm{a(T)\,n^*(r)\,n_H(r)} \cdot \frac{\mathrm{r}}{\mathrm{D}}\right)$$

Which brings us after some conversions to the final result of the model. Thus the differential equation is as follows:

$$\frac{\mathrm{d\,n^*}}{\mathrm{n^*}} \;=\; -\,\mathrm{dr}\left[2\,\mathrm{a(T)\,n_H(r)}\,\frac{\mathrm{r}}{\mathrm{D}} \;+\; \frac{1}{\mathrm{r}}\right] \tag{9}$$

Since we do not have a functional expression for the right-hand side of the equation and so it cannot be solved analytically in this form, the following simplifications are made for further steps:

$$\mathrm{F(r)} \;=\; 2\,\mathrm{a(T)\,n_H(r)}\,\frac{\mathrm{r}}{\mathrm{D}} \;+\; \frac{1}{\mathrm{r}} \tag{10}$$

$$\mathrm{I(r)} \;=\; \int \left[2\,\mathrm{a(T)}\,\mathrm{n_H(r)}\,\frac{\mathrm{r}}{\mathrm{D}} \;+\; \frac{1}{\mathrm{r}} \right] \mathrm{dr} \tag{11}$$

We can now solve the equation with the following steps:

$$\int \frac{\mathrm{d\,n^*}}{\mathrm{n^*(r)}} \;=\; -\,\mathrm{I(r)}$$

$$\ln\left(\frac{\mathrm{n^*(r)}}{\mathrm{n_0^*}}\right) \;=\; -\,\mathrm{I(r)}$$

$$\mathrm{n^*(r)} \;=\; \mathrm{n_0^*} \cdot \mathrm{e^{-I(r)}} \tag{12}$$

12 describes the decrease of the particle density, and thus the annihilation, after the positrons have passed the edges of the Local Bubble. Inside, a constant density is assumed with $\mathrm{n_0^*}$, which depends only on the activity of the $^{26}\mathrm{Al}$. In the following we will have a look at the function F(r) and its antiderivative I(r) in order to appproximate their shapes by analytical functions.

4.2.1 Solution of the differential equation

To approximate the functions F(r) and I(r), a representation of the annihilation rates as a function of the radius of the Local Bubble must be found. For this purpose, the underlying temperature-dependent rates from Fig. 6 are used. These are computed with the temperature distribution (Fig. 18) of the positrons in order to represent the annihilation rates as a function of the radius ($\mathrm{a(T)} \rightarrow \mathrm{a[T(r)]}$).
Fig. 19 shows the annihilation rates obtained. The processes of charge exchange (Sec. 2.3.1), of direct annihilation (Sec. 2.3.3) and of radiative recombination (Sec. 2.3.2) are shown. It can be seen that the charge exchange dominates by three orders of magnitude. The last plot (bottom right) shows the total annihilation coefficient. We see the shape of Fig. 6 when adding the coefficients for charge exchange, radiative recombination and direct annihilation. We see that inside the Local Bubble the annihilation rates are 5 magnitudes of order lower than in the shell. Thus, the total annihilation rate is approximately equal to that of the charge exchange. The conclusion is that the positrons in the outer regions annihilate mainly through this process.
Using these annihilation rates, the function F(r) can now be represented according to equation 10. The result is shown in Fig. 20:
It can be seen that at a radius of $\mathrm{r_{m,0}} = 155.1\,\mathrm{pc}$ the annihilation of positrons becomes efficient due to the start of the charge exchange ($\mathrm{T} \sim 6 \cdot 10^6\,\mathrm{K}$). For $\mathrm{F(r < r_{m,0})}$, the function is three orders of magnitude smaller and thus irrelevant (direct annihilation, radiative recombination).

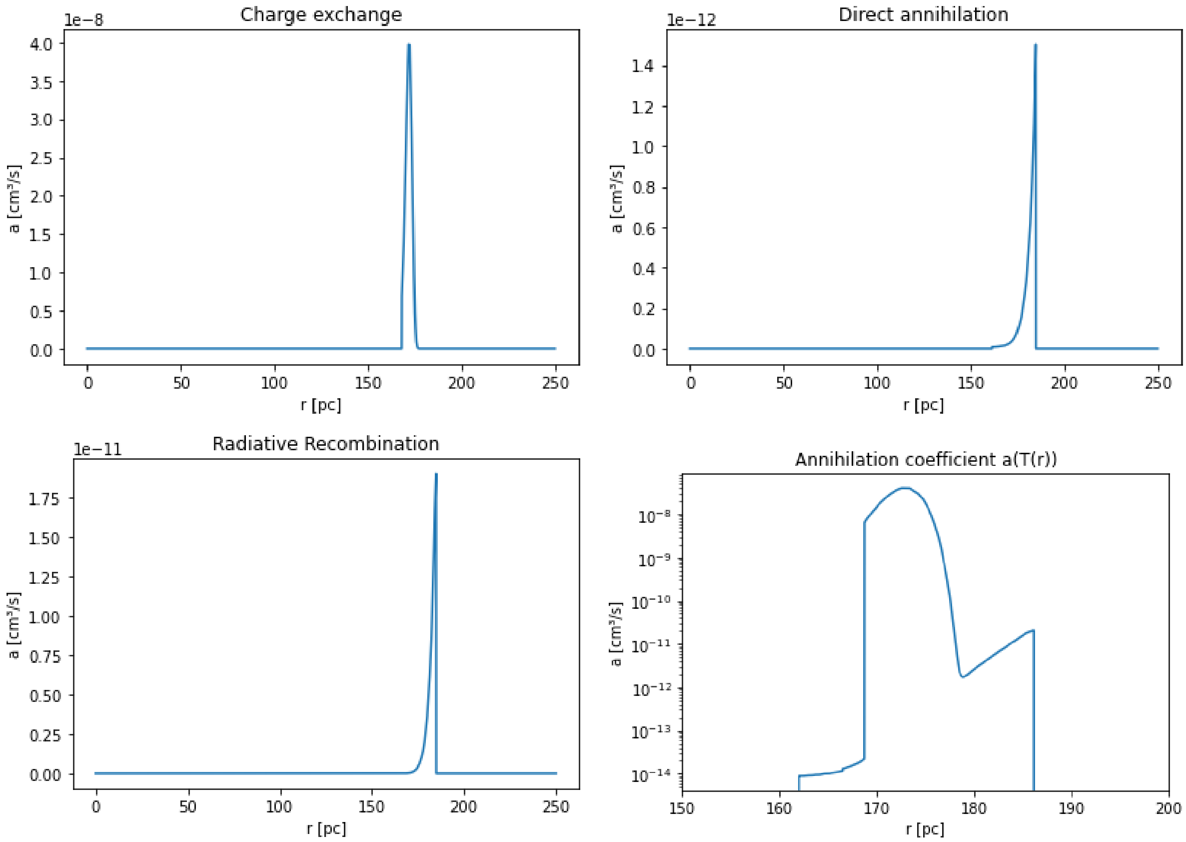

Fig. 19: Annihilation rates as a function of the radius of the Local Bubble. The rates of the individual processes are shown, as well as the total annihilation rate (bottom right).

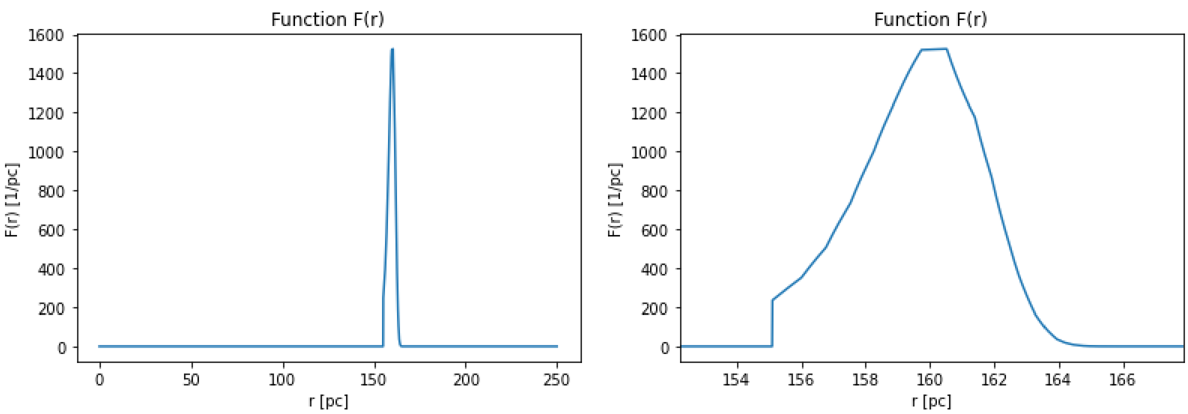

Fig. 20: The function F(r) for the whole Local Bubble (left) and in the region of (152 - 168) pc (right).

The next step is to find an expression for the description of F(r). Only the range where $\mathrm{r} \geq \mathrm{r}_{\mathrm{m},0}$ is used for this approximation. For this purpose an asymmetric Gaussian function is used. It has the following form:

$$\mathrm{F(r)} \;=\; \sqrt{\frac{\pi}{2}} \cdot \frac{\mathrm{A} \cdot \sigma}{\tau} \cdot \exp\left(\frac{2\tau\,(\mathrm{r}-\mu)\;+\sigma^2}{2\tau^2}\right) \mathrm{erfc}\left(\frac{\tau(\mathrm{r}-\mu)\;+\;\sigma^2}{\sqrt{2}\sigma\tau}\right)$$

A is the amplitude of a Gaussian function, μ is the center, σ the width and $\tau > 0$

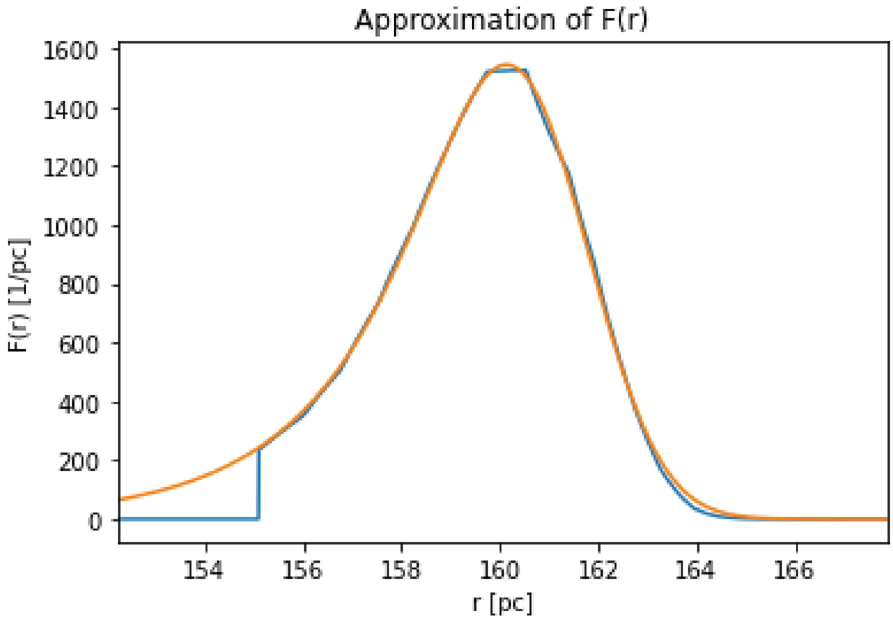

Fig. 21: Approximation of F(r) in blue with the help of an assymetric Gaussian function in orange.

the assymetry parameter. It can be seen in Fig. 21 that an approximation of F(r) with the asymmetric Gaussian function is adequate. The aprroximation parameters are: $A = 2.38 \cdot 10^3\,\mathrm{pc}^{-1}$, $\mu = 1.61 \cdot 10^2\,\mathrm{pc}$, $\sigma = 1.30\,\mathrm{pc}$ and $\tau = 2.17$. Thus an analytical, integrateable function was found to replace the part of the differential equation (9) which cannot be solved analytically. By integration of the function F(r) we arrive in the next step at the function I(r), with which we finally arrive at the positron distribution function 12.

$$\mathrm{I(r)} = \int \mathrm{F(r)\,dr}$$

$$\mathrm{I(r)} = \sqrt{\frac{\pi}{2}}\,\frac{\mathrm{A}\sigma}{\tau} \int_{\mathrm{r_{m,0}}}^{\infty} \exp\left(\frac{2\tau\,(\mathrm{r}-\mu) + \sigma^2}{2\tau^2}\right) \mathrm{erfc}\left(\frac{\tau(\mathrm{r}-\mu) + \sigma^2}{\sqrt{2}\sigma\tau}\right) \mathrm{dr}$$

Here we integrate from $r_{m,0}$ to infinity, because exactly here is the volume in which the annihilations take place and the function thus describes the path of the positrons. Thus one receives:

$$\mathrm{I(r)} = \sqrt{\frac{\pi}{2}}\frac{\mathrm{A}\sigma}{\tau} \cdot \left[\tau \exp\left(\frac{2\tau\,\mathrm{r} - 2\mu\tau + \sigma^2}{2\tau^2}\right) \mathrm{erfc}\left(\frac{\tau(\mathrm{r}-\mu)+\sigma^2}{\sqrt{2}\sigma\tau}\right) + \tau\,\mathrm{erfc}\left(\frac{\mu - \mathrm{r}}{\sqrt{2}\sigma}\right)\right.$$

$$\left. - \tau \exp\left(\frac{2\tau\,\mathrm{r_{m,0}} - 2\mu\tau + \sigma^2}{2\tau^2}\right) \mathrm{erfc}\left(\frac{\tau(\mathrm{rm}-\mu)+\sigma^2}{\sqrt{2}\sigma\tau}\right) - \tau\,\mathrm{erfc}\left(\frac{\mu - _{\mathrm{m,0}}}{\sqrt{2}\sigma}\right)\right]$$

In Fig. 22, the function I(r) is shown in a semi-logarithmic scheme.

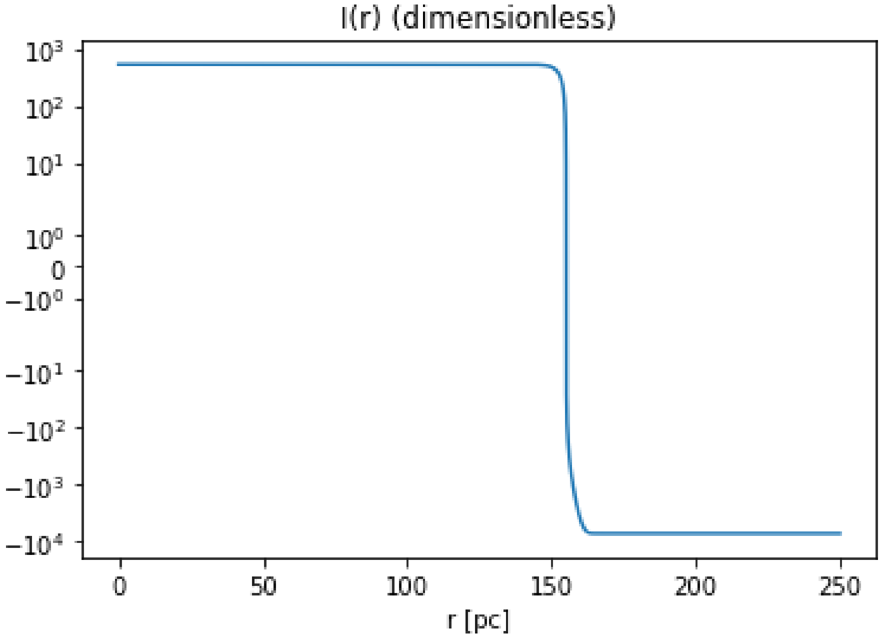

Fig. 22: The function I(r) computed as the integral of F(r). The zero point is at $r_{m,0}$ = 155.1 pc.

Finally the function I(r) is inserted into equation 12. Now we get the positron density depending on the radius of the Local Bubble. Fig. 23 shows $\mathrm{n}^*/\mathrm{n}_0$ this quantity. The radius $r_{m,0}$ depends on the radius of the Local Bubble and is calculated as follows:

$$\frac{\mathrm{r_{m,0}}}{\mathrm{r_0}} = \frac{155.1}{150} \cdot \mathrm{r}(\phi, \theta)$$

This calculation takes into account that, for an assumed radius of 150 pc, we observe annihilations starting at a radius $r_{m,0}$ of 155.1 pc and thus the decrease of the positron density, which is (nearly) constant in the interior. However, the Local Bubble itself has different edges depending on the viewing angle (Fig. 13) and thus different values for $r_{m,0}$.

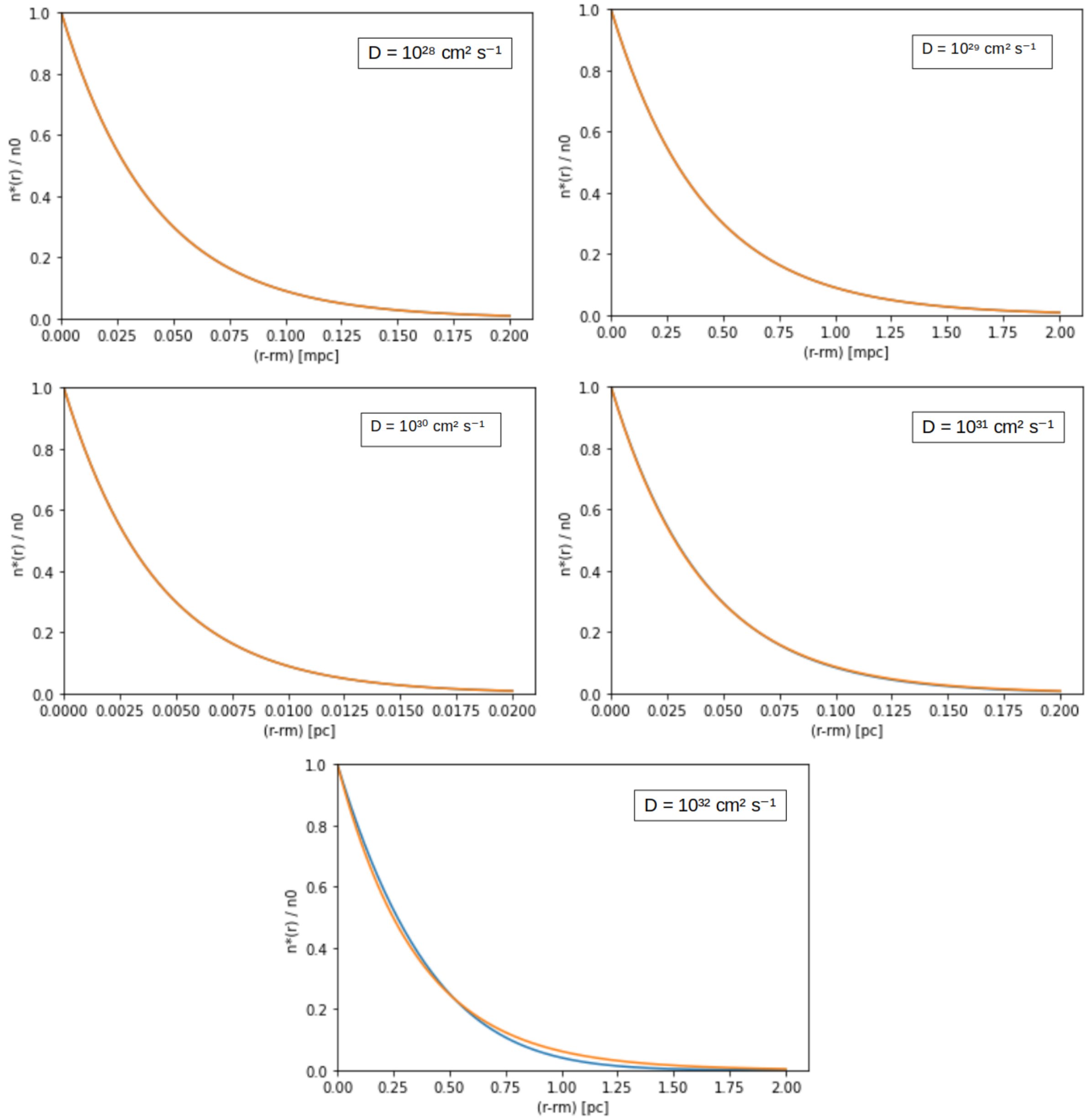

Fig. 23: Positron density distributions for D $= 10^{28}\,\mathrm{cm^2\,s^{-1}}$ up to D $= 10^{32}\,\mathrm{cm^2\,s^{-1}}$ (from top left to bottom) with the corresponding exponential functions.

Fig. 23 also shows that we described the positron density with an exponential function

$$\mathrm{n}^*(\mathrm{r}) = \mathrm{n}_0^* \cdot \exp\big(-\alpha \cdot \mathrm{r}\big) \tag{13}$$

with the values

$$\mathrm{D} = 10^{28}\,\mathrm{cm^2\,s^{-1}} \rightarrow \alpha = 2.41 \cdot 10^4\,\mathrm{pc^{-1}}$$

$$\mathrm{D} = 10^{29}\,\mathrm{cm^2\,s^{-1}} \rightarrow \alpha = 2.41 \cdot 10^3\,\mathrm{pc^{-1}}$$

$$\mathrm{D} = 10^{30}\,\mathrm{cm^2\,s^{-1}} \rightarrow \alpha = 2.43 \cdot 10^2\,\mathrm{pc^{-1}}$$

$$\mathrm{D} = 10^{31}\,\mathrm{cm^2\,s^{-1}} \rightarrow \alpha = 2.45 \cdot 10^1\,\mathrm{pc^{-1}}$$

$$D = 10^{32}\,\mathrm{cm^2\,s^{-1}} \rightarrow \alpha = 2.60\,\mathrm{pc^{-1}}$$

We see the different sizes of the annihilating shell for different diffusion coefficients.
It shows that all positrons annihilate within a very small range between $2 \cdot 10^{-4}$ to $2 \cdot 10^{0}$ pc. The higher D is, the larger the range. This result is consistent with the expectation that a higher diffusion coefficient can carry the particles further out before they finally annihilate. The model as a whole shows that the positrons from the interior of the local bubble first hit its shell with almost all their kinetic energy before they are abruptly decelerated due to the high particle density. In the end, they all annihilate within a thin shell near the edge of the Local Bubble.
We also simulated the positron propagation for low diffusion coefficients $D < 10^{28}\,\mathrm{cm^2\,s^{-1}}$. For all of these our model provided no annihilation at the edges of the Local Bubble. We assumed the random walk to calculate the energy loss and so the range of the positrons with equation 6. The characteristic length L is direct proportional to D. For low diffusion coefficients the random walk is thus to small to reach low temperatures of $\sim 5 \cdot 10^{6}\,\mathrm{K}$ at the edges of the Local Bubble. As a consequence the positrons propagate into adjacent superbubbles.

5 Gamma Ray Flux Expectations

In this chapter, we will use the above-described model to determine the gamma ray flux due to positron annihilation at the edge of the Local Bubble. For these calculations, we use the method of line of sight integration.

5.1 The method of line of sight integration

The line of sight integration calculates the total flux received from a point in the sky, i.e. along the entire ray up to infinity. This depends on the viewing angle of the observer. The flux is obtained by integration over an emissivity ρ which describes the number of photons created per unit time per unit volume. When scanning the complete sky with all its possible lines of sight and add all values, the total flux in the whole sky is obtained. In order to create a pixellated image of the whole sky, we define a pixel size in a cartesian grid. The larger this is, the more coarse-grained is the resolution of the calculation. With a lower binsize, on the other hand, we obtain sharper images of the entire sky. Given the angular resolution of current and future gamma-ray telescopes on the order of degrees, and for testing our models against the Galactic background (Chp. 6), we adapt a pixel size of 3° throughout this thesis.

$$\Delta\phi = \Delta\theta = 3^\circ$$

The integral itself for a fixed viewing angle has the following form:

$$\mathrm{F}(\phi, \theta) = \frac{1}{4\pi} \int_0^\infty \rho(\mathrm{r}(\mathrm{s}); \phi, \theta) \, \mathrm{ds} \tag{14}$$

5.2 Calculation of the annihilation emissivity

Before the line of sight integration can be performed, the photon emissivity must be determined. For this we first consider the positron emissivity, which we get from the radioactive decay of ^{26}Al. The activity of a radioactive isotope at time t is given by:

$$\mathrm{A(t)} \, = \, \lambda \cdot \mathrm{N_0} \cdot \exp\big(-\lambda \cdot \mathrm{t}\big)$$

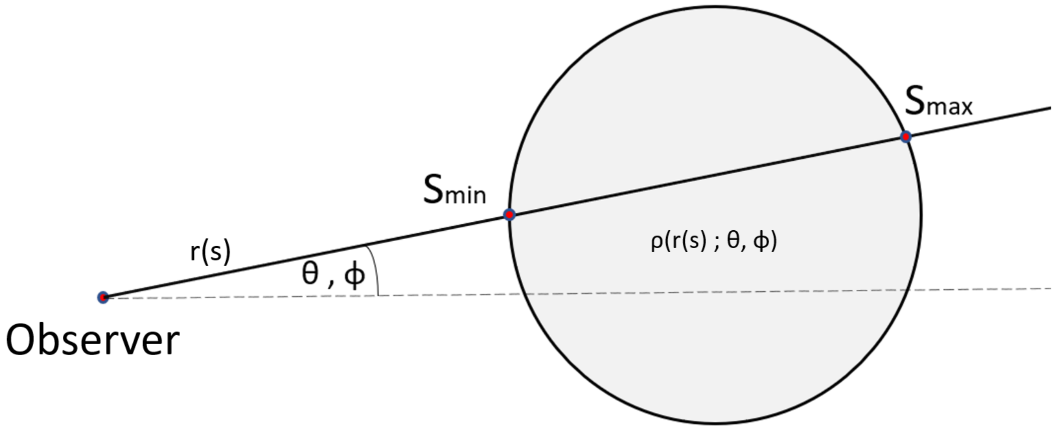

Fig. 24: Schematic representation of the line of sight integral. The observer is viewing along the line of sight s at the angle θ, ϕ. At a distance $r(s) = S_{min}$ is an object with an emissivity $\rho\big(r(s)\,;\,\phi,\theta\big)$. The outer radius of the object is S_{max}. In this case the line of sight integral is $\mathrm{F}(\phi,\theta) = \frac{1}{4\pi}\int_{S_{min}}^{S_{max}} \rho(r(s);\phi,\theta)\,ds$

Here λ is the decay constant and is given by the half life $\mathrm{T}_{1/2}$:

$$\lambda \;=\; \frac{\ln(2)}{\mathrm{T}_{1/2}}$$

N_0 is the initial number of nuclei of the isotope. This number is obtained by

$$\mathrm{N}_0 \;=\; \frac{\mathrm{M}}{\mathrm{m}}$$

with M beeing the yield of ^{26}Al from the supernova and m is the molar mass of the isotope. In our case, the equation must be multiplied by the branching ratio p for β^+ decay of of 0.82. Dividing this activity by the effective volume $\mathrm{V_{eff}}$ of the Local Bubble gives the positron emissivity

$$\rho_{\mathrm{po}}(\mathrm{M},\mathrm{t}) \;=\; \mathrm{p}\cdot\lambda\cdot\frac{\mathrm{M}}{\mathrm{m}}\cdot\exp\big(-\lambda\cdot\mathrm{t}\big)\cdot\frac{1}{\mathrm{V_{eff}}} \tag{15}$$

$$\mathrm{V_{eff}} \;=\; \int \mathrm{d}\Omega \int\limits_0^{\mathrm{R}(\phi,\theta)} \mathrm{s}^2\,\mathrm{p(s)}\,\mathrm{ds} \tag{16}$$

The effective volume is given by the geometry of any emissivity profile $p(s)$ and describes the normalization to the luminosity. If the region of interest is not sharply defined, such as in our case with the Local Bubble, but rather infinitely extended, such as an exponential profile, the effective volume acts as a finite emission region. From this positron emissivity the annihilation emissivity can be determined. At first the positron density is obtained for which an equation was set up in the chapter 4. The in our model constant positron density in the inner n_0^* is determined by

$$n_0^* = \rho_{po}(M, t) \cdot \tau \tag{17}$$

where τ is the characteristic time scale between production and annihilation of a positron. Here τ is calculated by the time the positrons need to travel to the outside of the Local Bubble.

$$\tau = \frac{R(\phi, \theta)}{v_{in}}$$

$R(\phi, \theta)$ is radius in dependence of the solid angle and v_{in} the initial velocity of the positrons (543.3keV $\rightarrow$ 0.87c). The positron density at the edge, where we observe annihilations, now has the following form according to the equation 13:

$$n^*(r) = \rho_{po}(M, t) \cdot \frac{R(\phi, \theta)}{v_{in}} \cdot \exp\bigl(-\alpha \cdot r\bigr)$$

With each annihilation process the positron density changes but also the annihilation density. The two processes are inversely proportional to each other. In general, the annihilation emissivity is estimated by the non-steady state solution of equation 8. We approximated the solution by assuming, that the change in positron density occurs only via annihilation. Therefore we derived four different methods from that point to obtain the annihilation emissivity.

A) Describing the positrons as ballistic particles

If we assume that almost all annihilation processes take place via charge exchange, we have a positronium fraction $f_{ps} = 1$. Section 2.3.4 shows that oPs is formed with a probability of 1/4 and we obtain two photons. In 3/4 of the cases, oPs is formed and we obtain 3 photons. The ratio between photons of 511 keV to photons going into the oPs spectrum for $f_{ps} = 1$ is $F_{511}/F_{oPs} = 1/4.5$ [Guessoum et al., 2005]. For the case of 511 keV we obtain two photons. We thus have to multiply our emissivity by

$$2 \cdot \frac{2}{11} = 0.36$$

$$\frac{d\,n^*}{dt} = -\rho_{anni} \cdot 0.36$$

$$\frac{d\,n^*}{dr} \cdot \frac{dr}{dt} = -\rho_{anni} \cdot 0.36$$

$$\frac{d\,n^*}{dr} \cdot v_{fin} = -\rho_{anni} \cdot 0.36$$

In the conversion steps shown, the time derivative is replaced by a derivative according to the radius multiplied by the final velocity of the positrons. The total photon emissivity is now:

$$\rho_{\mathrm{anni,1}} \;=\rho_{\mathrm{po}}(\mathrm{M,t})\cdot\frac{\mathrm{v_{fin}}}{\mathrm{v_{in}}}\cdot\alpha\cdot\mathrm{R}(\phi,\theta)\cdot\exp\big(-\alpha\cdot\mathrm{r}\big)\cdot 0.36 \tag{18}$$

During annihilation a final energy of 100 eV is assumed [Prantzos et al., 2011]. Thus the ratio $\mathrm{v_{fin}}/\mathrm{v_{in}}$ is 0.014. So the total photon emissivity ρ_{ph} depends only on two factors: the ejected mass of ^{26}Al and the time t which has passed since the supernova.

B) Describing annihilation time scale with diffusion coefficient

We can approximate τ, the annihilation time scale, by

$$\tau \;=\; \frac{2\cdot\mathrm{R}^2}{\mathrm{D}}$$

with R beeing the range in which the positrons annihilate, so that we get assuming to euqtaion 17

$$\mathrm{n}^*(\mathrm{r}) \;=\; \rho_{\mathrm{po}}(\mathrm{M,t})\cdot\tau\cdot\exp\big(-\alpha\cdot\mathrm{r}\big)$$

$$\mathrm{n}^*(\mathrm{r}) \;=\; \rho_{\mathrm{po}}(\mathrm{M,t})\cdot\frac{2\cdot\mathrm{R}^2}{\mathrm{D}}\cdot\exp\big(-\alpha\cdot\mathrm{r}\big)$$

We can now again say that 36% of the flux is going into 511 keV that

$$\frac{\mathrm{d\,n}^*}{\mathrm{dr}}\cdot\mathrm{v_{fin}} \;=\; -\,\rho_{\mathrm{anni}}\cdot 0.36$$

with $\mathrm{v_{fin}}$ beeing $\mathrm{D}/(2\cdot\mathrm{R})$. The obtained emissivity now looks as follows:

$$\rho_{\mathrm{anni,2}} \;=\; \rho_{\mathrm{po}}(\mathrm{M,t})\cdot\alpha\cdot\mathrm{R}(\phi,\theta)\cdot\exp\big(-\alpha\cdot\mathrm{r}\big)\cdot 0.36 \tag{19}$$

In this case R as the 'annihilation range' changes with the diffusion coefficient D. For example, for $\mathrm{D} = 10^{32}$ we obtain $\frac{\mathrm{n}^*}{\mathrm{n}_0} = 1\%$ at $\mathrm{R} = 1\,\mathrm{pc}$ (Fig. 23).

C) Replacing the time derivative by the annihilation time scale

In this method we replace the time derivative $\mathrm{dn}^*/\mathrm{dt}$ by characteristic time scale τ_{tot}.

$$\frac{\mathrm{d\,n}^*}{\mathrm{dt}} \;=\; \frac{\mathrm{n}^*}{\tau_{\mathrm{tot}}}$$

$$\tau_{\mathrm{tot}} \;=\; \tau_{\mathrm{cool}} \;+\; \tau_{\mathrm{anni}}$$

Herefore, we now need to estimate the annihilation time scale τ_{anni} (how much time do positrons need to annihilate after they cooled down) and the cooling time τ_{cool} (how much time do the positrons need to cool down from a certain initial energy). In general, τ_{anni} is

$$\tau_{\mathrm{anni}} = \frac{1}{\sigma \cdot \mathrm{v} \cdot \mathrm{n_H}}$$

where σ is the annihilation cross section, v is the final positron velocity and n_H is the density of the ambient medium. τ_{anni} then becomes a function of the final positron energy because v and also σ depend on this. Fig. 25 shows the cross section for positronium formation via charge exchange (blue). For an estimated final energy of 100 eV, we obtain $\sigma = 10^{-18}\,\mathrm{cm}^2$, $\mathrm{v} = 6 \cdot 10^8\,\mathrm{cm\,s^{-1}}$ and $\mathrm{n_H} = 15\,\mathrm{cm}^{-3}$. Therefore we obtain $\tau_{\mathrm{anni}} = 10^8\,\mathrm{s}$.

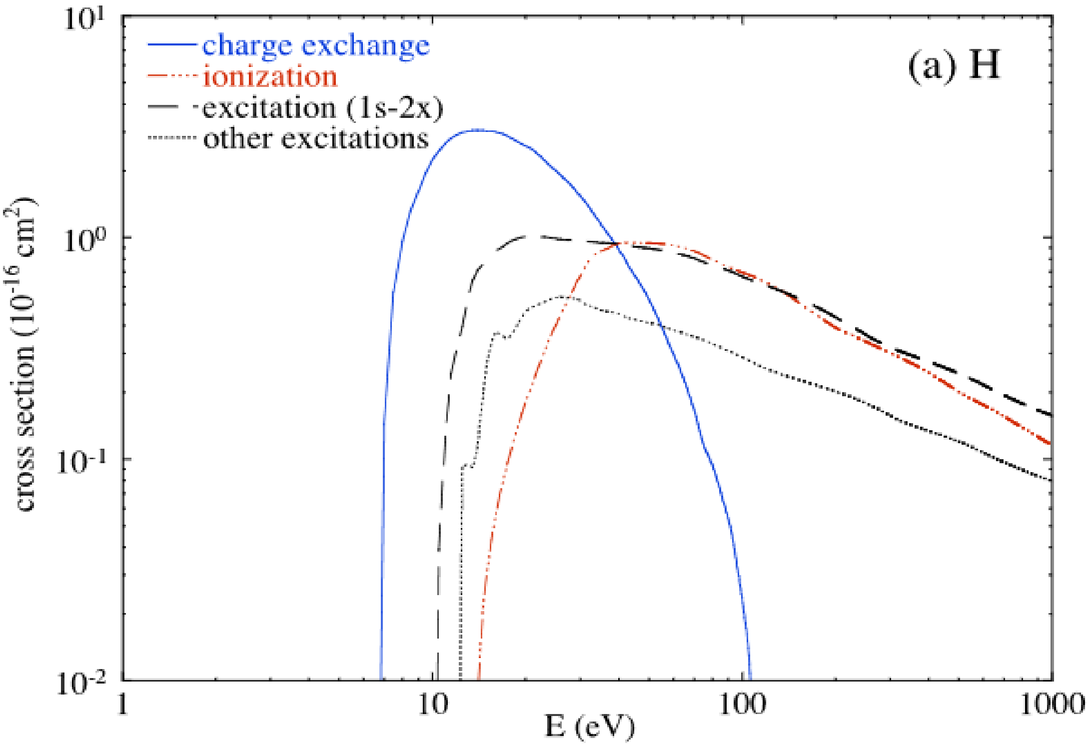

Fig. 25: Cross sections for positronium formation, ionization and excitation in positron collision with atomic hydrogen [Guessoum et al., 2005]

We now also have to estimate the cooling time scale τ_{cool}. Therefore we calculate the cooling time from a certain initial energy to a final zero energy.

$$\tau_{\mathrm{cool}} = \int_{\mathrm{E_{in}}}^{0} \frac{\mathrm{dE}}{\left|\frac{\mathrm{dE}}{\mathrm{dt}}\right|}$$

We did this for the energy band of 0 eV to 1,1 MeV with a step-size of 10 keV cause all the positrons are created within this energy band. Fig. 26 shows the resulting cooling time τ_{cool} in dpendence of the positrons initial energy. We can see that for higher values of E_{max} also the time rises as we expect.

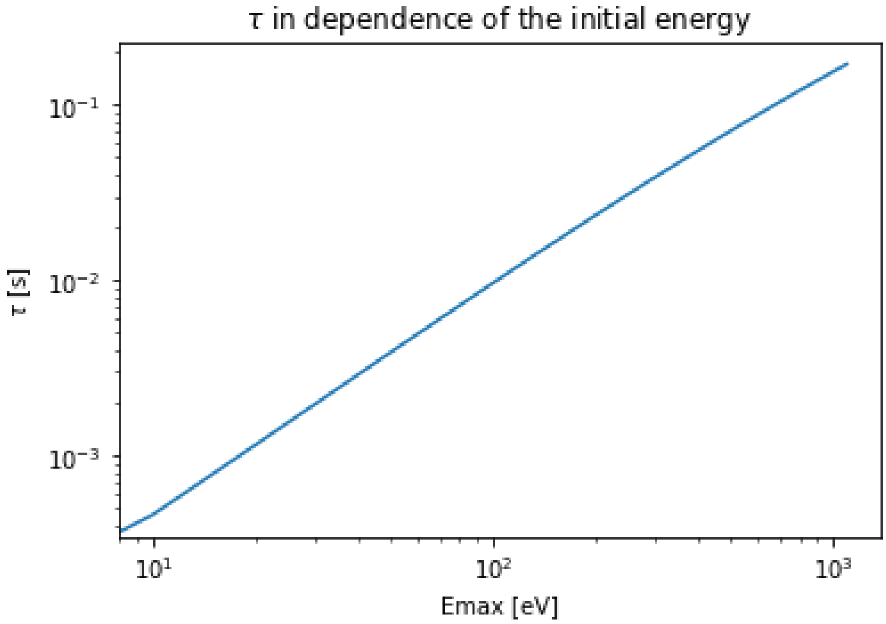

Fig. 26: τ_{cool} for different values of the initial energy E_{max} of the positrons.

We now have to weight these values with the help of the β^+-decay spectrum. There is no data for the decay spectrum of ^{26}Al. So, we approximated the spectrum by a parabola with the peak at 550 keV (mean energy) and its zeros at 0 eV and 1100 keV (maximum energy). Fig. 27 shows the parabola calculated by

$$(\mathrm{E_{max}} \;=\; \mathrm{B} \cdot (\mathrm{E_{max}} \;-\; 1100\,\mathrm{kev}) \cdot \mathrm{E_{max}}$$

where

$$\mathrm{B} \;=\; \frac{10^{-3}}{550^2}\,\frac{1}{\mathrm{keV}^2}$$

Weighting the values of τ_{cool} with the parabola is shown in Fig. 28.
Out of this we can now calculate the mean value of τ_{cool} by

$$\langle \tau_{\mathrm{cool}} \rangle \;=\; \frac{\sum \tau_{\mathrm{cool}}(\mathrm{E_{max}}) \cdot \mathrm{f}(\mathrm{E_{max}})}{\sum \mathrm{f}(\mathrm{E_{max}})}$$

which gives us

$$\langle \tau_{\mathrm{cool}} \rangle \;=\; 0.080\,\mathrm{Myr} \;=\; 2.51 \cdot 10^{12}\,\mathrm{s}$$

We see that the cooling time scale τ_{cool} is much lager than the annihilation time scale τ_{anni} calculated before. We thus set

$$\tau_{\mathrm{tot}} \;=\; \tau_{\mathrm{cool}} \;+\; \tau_{\mathrm{anni}} \;=\; \tau_{\mathrm{cool}} \;=\; 0.080\mathrm{Myr}$$

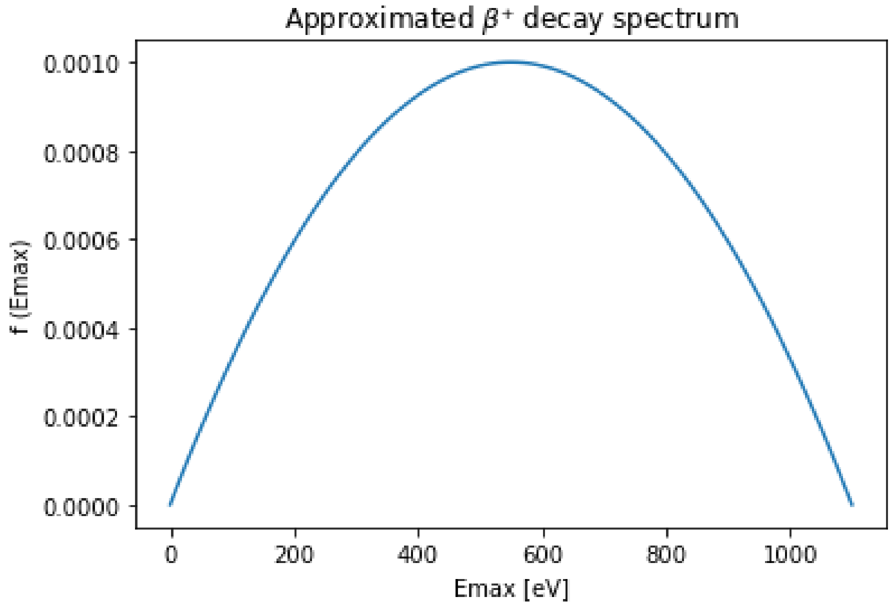

Fig. 27: Parabola for approximating the β^+ decay spectrum.

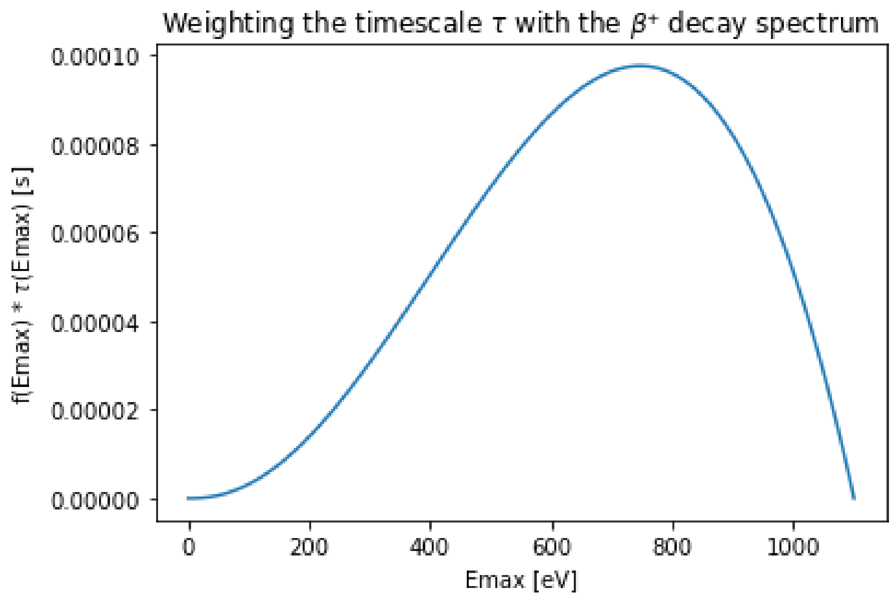

Fig. 28: τ_{cool} values weighted by the approximated β^+ decay spectrum.

We finally get the emissivity

$$\rho_{\mathrm{anni,3}} = \rho_{\mathrm{po}}(\mathrm{M,t}) \cdot \frac{\mathrm{R}(\phi, \theta)}{\tau_{\mathrm{cool}} \cdot \mathrm{v_{fin}}} \cdot \exp\big(-\alpha \cdot \mathrm{r}\big) \cdot 0.36 \tag{20}$$

D) Calculation by considering the time difference between positron formation and annihilation

The positron emissivity inside the Local Bubble is given by equation 15

$$\rho_{\rm po}({\rm M,t}) \;=\; {\rm p}\cdot\lambda\cdot\frac{\rm M}{\rm m}\cdot\exp\big(-\lambda\cdot{\rm t}\big)\cdot\frac{1}{\rm V_{eff}}$$

These positrons move diffusively until they thermalize with the ISM and annihilate with electrons. This again takes the time

$$\tau_{\rm tot} \;=\; \tau_{\rm cool} \;+\; \tau_{\rm anni}$$

with τ_{cool} beeing the timescale of the positrons losing their energy, e.g. cooling to low temperatures and τ_{anni} beeing the annihilation time scale (Sec. 5.2). Thus the number of positrons annihilating and the number of positrons forming are delayed by τ_{tot}. We estimated the annihilation emissivity out of the positron emissivity as now follows:

$$\rho_{\rm anni} \;=\; \rho_{\rm po}\cdot\exp\big(\lambda\cdot\tau_{\rm tot}\big)$$

Finally, we multiply the emissivity with the profile n^*/n_0 due to equation 13. Our result is now

$$\rho_{\rm anni,4} \;=\; \rho_{\rm po}\cdot\exp\big(\lambda\cdot\tau_{\rm tot}\big)\cdot\cdot\exp\big(-\alpha\cdot{\rm r}\big)\cdot 0.36 \tag{21}$$

5.3 Expected gamma ray flux

We now insert the determined emissivity into the line of sight integral and thus calculate the photon flux, which we obtain from the annihilation of positrons in the Local Bubble. For the edges of the Local Bubble we assume a multipole expansion up to i=3 (Fig. 13). The pixel size is $3^\circ \times 3^\circ$. For the initial mass M of ^{26}Al we choose a yield of $7.5\cdot 10^{-5}\,\mathrm{M}_\odot$ [Bauer, N.; priv. comm.]. For the time t, which has passed since the supernova, we assume 3 Myr [Chaikin et al., 2022].

5.3.1 General results

Fig 29 shows the all-sky flux map of positron annihilation obtained by the line of sight integration using Galactic coordinates. The effective volume from equation 16 is $0.046\,\mathrm{kpc}^3$. The total all-sky integrated annihilation flux is $1.3\cdot 10^{-5}\,\mathrm{ph\,cm^{-2}\,s^{-1}}$ taking into account the branching ratio (82%) of the β^+ decay, the fraction (18%) of photons going into the 511 keV line due to positronium formation and the 2 photons we obtain in the case of 511 keV emission. The structure of the Local Bubble is clearly visible. We get a larger flux from the areas that have smaller radii. This is due to the fact that the positrons annihilate in a small shell around the Local Bubble. The flux decreases with the square of the distance to the source, which is why we obtain a higher flux for more nearby edges. We can see the bright spot that is nearly in the center. Here the Local Bubble has a dent

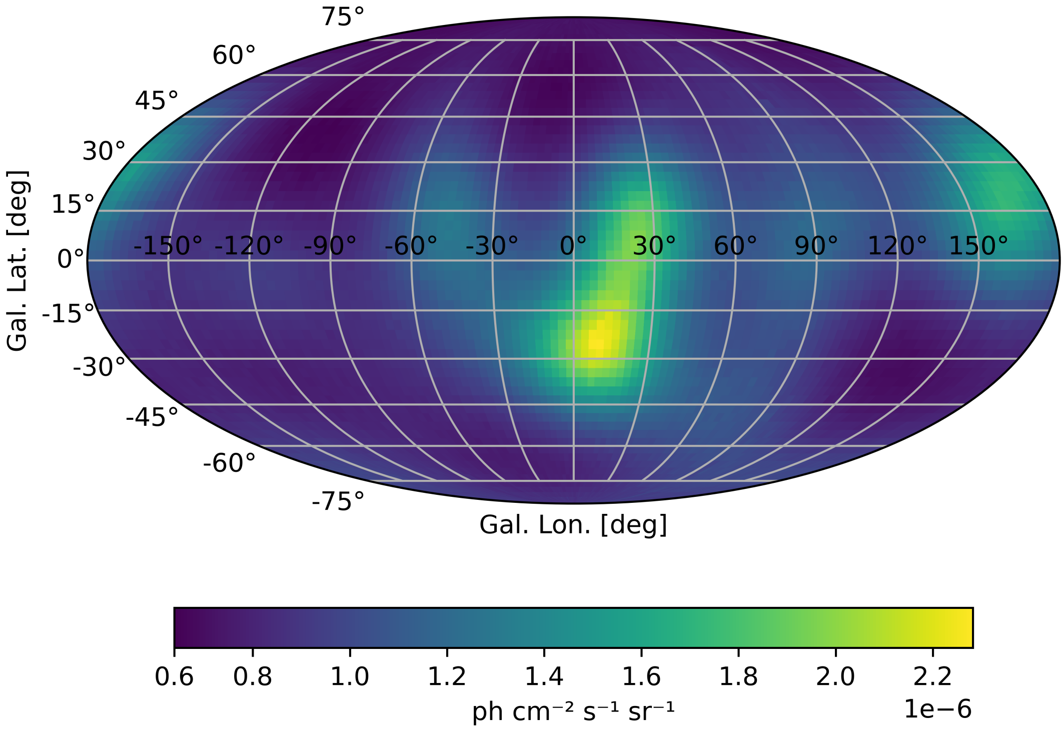

Fig. 29: Calculated positron annihilation flux map with emissivity according to equation 18. The pixel size is $3 \times 3\,\mathrm{deg}^2$. The different radii of the Local Bubble were taken into account.

(smallest radii of $\sim 90-100$ pc) which makes this region very prominent in the flux map. Since we obtain a flux in every square pixel of the sky, the Local Bubble shows an isotropic flux contribution. Subtracting the minimum flux value from the all-sky map, gives us the unisotropic fraction. This unisotropic contribution is shown in Fig. 30.

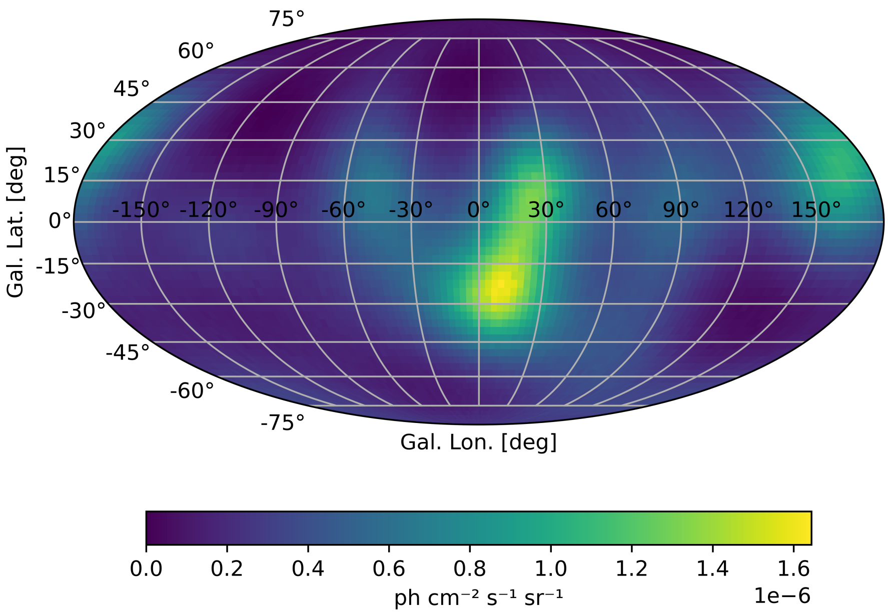

Fig. 30: Unisotropic part of the Local Bubble annihilation flux.

We can also calculate the isotropic part of the total flux, which is $8.5 \cdot 10^{-6}\,\mathrm{ph\,cm^{-2}\,s^{-1}}$, meaning that 65% of the total flux is isotropic.

5.3.2 Variations with diffusion coefficient

As described in Sec. 4.1.2, the diffusion coefficient is unknown for low-energy positron transport in the ISM. We tested different assumptions for this reason with diffusion coefficient range of $10^{22}\,\mathrm{cm^2\,s^{-1}}$ to $10^{32}\,\mathrm{cm^2\,s^{-1}}$. Therefore we found out that for $D < 10^{28}$ the positrons do not annihilate in the shell of the Local Bubble. They lose their kinetic energy very slow and thus propagate into neighbouring superbubbles (Sec. 4.2). For the remaining diffusion coefficients $10^{28}\,\mathrm{cm^2\,s^{-1}} - 10^{32}\,\mathrm{cm^2\,s^{-1}}$ just the steepness of the declining positron density changes.

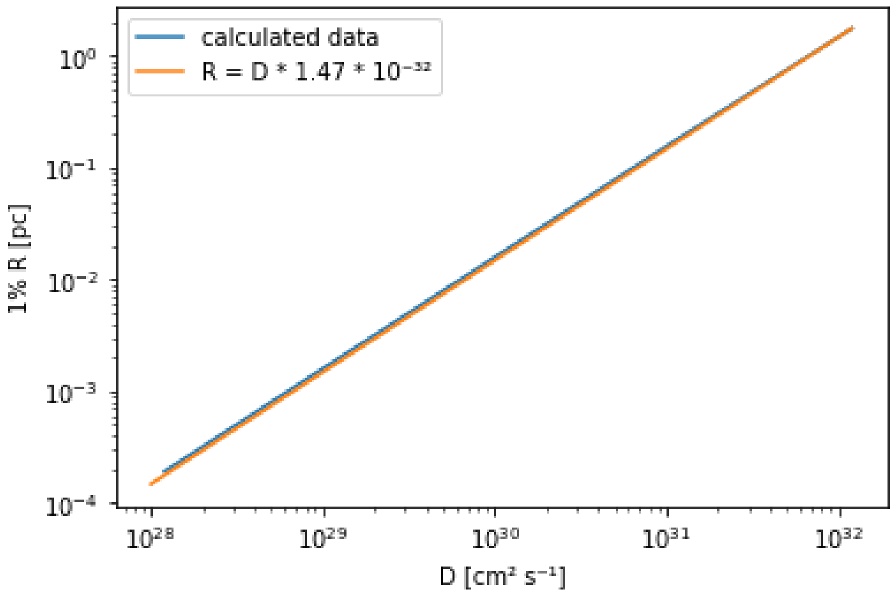

Fig. 31: Radius R of positron annihilation shell in dependence of D.

Fig. 31 shows the D dependence of the positron annihilation shell. It can be described as

$$\mathrm{R} = \mathrm{D} \cdot \mathrm{C}$$

where $\mathrm{C} = 1.47 \cdot 10^{-32}$. However, the total flux inside the shell is nearly constant for different diffusion coefficients. The total flux over the entire sky will not change cause $\mathrm{R_{shell}/R_{LB}} < 1\,\%$.

5.3.3 Systematic uncertainties

While the diffusion coefficient means a big uncertainty in the positron density profiles shape, the total annihilation flux remains constant. A very large uncertainty for the

flux comes from the ejected mass of ^{26}Al, the time of the injection and the charakteristic time scale τ_{cool} and τ_{anni} after thermalization. The ejected ^{26}Al mass is a linear parameter in the emissivity, and thus also in the annihilation flux. Given the expected range of $2 \cdot 10^{-5} - 12 \cdot 10^{-5}\,\mathrm{M}_{\odot}$, the flux may change between $3.4 \cdot 10^{-6}\,\mathrm{ph\,cm^{-2}\,s^{-1}}$ and $2.2 \cdot 10^{-5}\,\mathrm{ph\,cm^{-2}\,s^{-1}}$. The time of the last supernova explosion can be roughly estimated as 3 Myr ago. On the other hand, ocean crust measurements to determine the ^{60}Fe influx on earth reveal a time period of 1 Myr. Calculating the flux with a range in time of 2.5-3.5 Myr provides a range in flux of $7.8 \cdot 10^{-6}\,\mathrm{ph\,cm^{-2}\,s^{-1}}$ to $2.0 \cdot 10^{-5}\,\mathrm{ph\,cm^{-2}\,s^{-1}}$.
Finally, we calculated the cooling down (from ionization losses) and the annihilation timescales (Sec. 5.2). The cooling down timescale τ_{cool} is 3-4 magnitudes of order larger than the annihilation timescale τ_{anni}, so that we can ignore τ_{anni}. τ_{cool} changes between 0.171 Myr for the maximum kinetic energy of the β^{+} decay, 1.1 MeV, over 0.078 Myr for 543.3 keV (mean energy) to basically zero for the lower end of the spectrum. These different values give an additional uncertainty of

$$\exp\left(\lambda \cdot \tau_{\mathrm{cool,\,max}}\right) \;=\; \exp\left(\lambda \cdot 0.171\,\mathrm{Myr}\right) \;=\; 1.179 \;=\; 18\% \tag{22}$$

5.3.4 Variations with different emissivities

In general, the emissivity is calculated by the non-steady-state $\mathrm{dn}^{*}/\mathrm{dt} \neq 0$. This change of the positron density has different scales, the contribution of which we cannot estimate. Thus, only by knowing the full initial conditions and the evolution parameters of a superbubble over time could we calculate $\mathrm{dn}^{*}/\mathrm{dt}$. Therefore, we have estimated the annihilation emissivities using four different approaches. We compare the obtained annihilation fluxes with the same-time ^{26}Al flux of $3.5 \cdot 10^{-6}\,\mathrm{ph\,cm^{-2}\,s^{-1}}$ for an initial ^{26}Al mass of $7.5 \cdot 10^{-5}\,\mathrm{M}_{\odot}$ [Bauer,N; priv comm.]. We multiply this value by the various factors describing the uncertainties between ^{26}Al flux and annihilation flux: $\mathrm{X}_1 = 1.18$ from the uncertainty coming from τ_{cool}, the characteristic cooling time scale for the positrons (Eq. 22), $\mathrm{X}_2 = 2$ for the two photons we obtain for 511 keV emission, $\mathrm{X}_3 = 0.82$ considering the branching ratio of the β^{+} decay and $\mathrm{X}_4 = 0.18$ for the fraction of photons going into the 511 keV for the case of positronium formation. Finally, the expected annihilation flux is:

$$\mathrm{f}_{511,1} \;=\; \mathrm{f}_{^{26}\mathrm{Al}} \cdot \mathrm{X}_1 \cdot \mathrm{X}_2 \cdot \mathrm{X}_3 \cdot \mathrm{X}_4 \;=\; 1.2 \cdot 10^{-6}\,\mathrm{ph\,cm^{-2}\,s^{-1}} \tag{23}$$

There is an addtional way to estimate the annihilation flux. The ^{26}Al mass of $7.5 \cdot 10^{-5}\,\mathrm{M}_{\odot}$ provides a positron number created in the last 3 Myr of

$$\mathrm{N}_{\mathrm{e}^{+}} \;=\; \frac{\mathrm{M}}{\mathrm{m}} \cdot \mathrm{p}\left(1 - \exp(-\lambda \cdot \mathrm{t})\right) \;=\; 2.7 \cdot 10^{51}$$

If we assume that all of these positrons annihilated continuously within the last 3 Myr, we can convert this into a positron flux by

$$\mathrm{f_{e^+}} \;=\; \frac{\mathrm{M}}{\mathrm{m}} \cdot \mathrm{p}\left(1 - \exp(-\lambda \cdot \mathrm{t})\right) \frac{1}{4\pi\,\mathrm{R}^2}\,\frac{1}{3\,\mathrm{Myr}} \;=\; 1.1 \cdot 10^{-5}\,\mathrm{e^+\,cm^{-2}\,s^{-1}}$$

where R is the average radius of the Local Bubble (150 pc). We now multiply this value by $2 \cdot 0.18$ to get the annihilation flux:

$$\mathrm{f_{511,2}} \;=\; 3.8 \cdot 10^{-6}\,\mathrm{ph\,cm^{-2}\,s^{-1}} \tag{24}$$

We will now compare the annihilation flux values obtained from the four emissivites with the estimated values. The first method describes the positrons within the annihilation shell as ballistic particles (Eq. 18). We get the above-mentioned flux of $1.3 \cdot 10^{-5}\,\mathrm{ph\,cm^{-2}\,s^{-1}}$. This variant agrees within one order of magnitude with $f_{511,2}$ but is more than one order of magnitude larger than $f_{511,1}$.

The second emissivity (Eq. 19) describes the positrons as diffusing particles. The corresponding flux is $4.9 \cdot 10^{-6}\,\mathrm{ph\,cm^{-2}\,s^{-1}}$, which agrees with both estimate values $f_{511,1}$ and $f_{511,2}$.

With the third method $\mathrm{dn^*/dt} \;=\; \mathrm{dn^*}/\tau_{\mathrm{cool}}$ and the corresponding emissivity (Eq. 20) we get a flux of $1.0 \cdot 10^{-7}\,\mathrm{ph\,cm^{-2}\,s^{-1}}$. This value does not agree with either of the two estimates and is thus considered unphysical. We see that the estimation of the integral $\mathrm{dn^*/dt} \;=\; \mathrm{dn^*}/\tau_{\mathrm{cool}}$ with the time scale τ_{cool} involves a high uncertainty.

The last method considers the time scale τ_{cool} between positron formation and annihilation. With the corresponding emissivity (Eq. 21) we get a flux of $1.5 \cdot 10^{-5}\,\mathrm{ph\,cm^{-2}\,s^{-1}}$. This value is in the range of the flux value obtained from the first method and agrees, just like the latter, with the estimate value $f_{511,2}$ within one order of magnitude.

All flux values of the different models were compared with the two estimate values. The best agreement is given by the model of diffusing positrons. the resulting annihilation flux value agrees with both estimates. From the comparison we draw the conclusion that we have to describe the positrons as diffusing particles also in the annihilation shell, in order to keep the uncertainties as small as possible.

5.4 Gamma ray flux of distant superbubbles

With the help of this line-of-sight integration, we also calculated the annihilation flux of distant superbubbles. We approximate these as perfect spheres. As free parameters we have the radius r of the sphere and the position (x, y, z) giving the distance d of the object:

$$\mathrm{d} = \sqrt{\mathrm{x}^2 + \mathrm{y}^2 + \mathrm{z}^2}$$

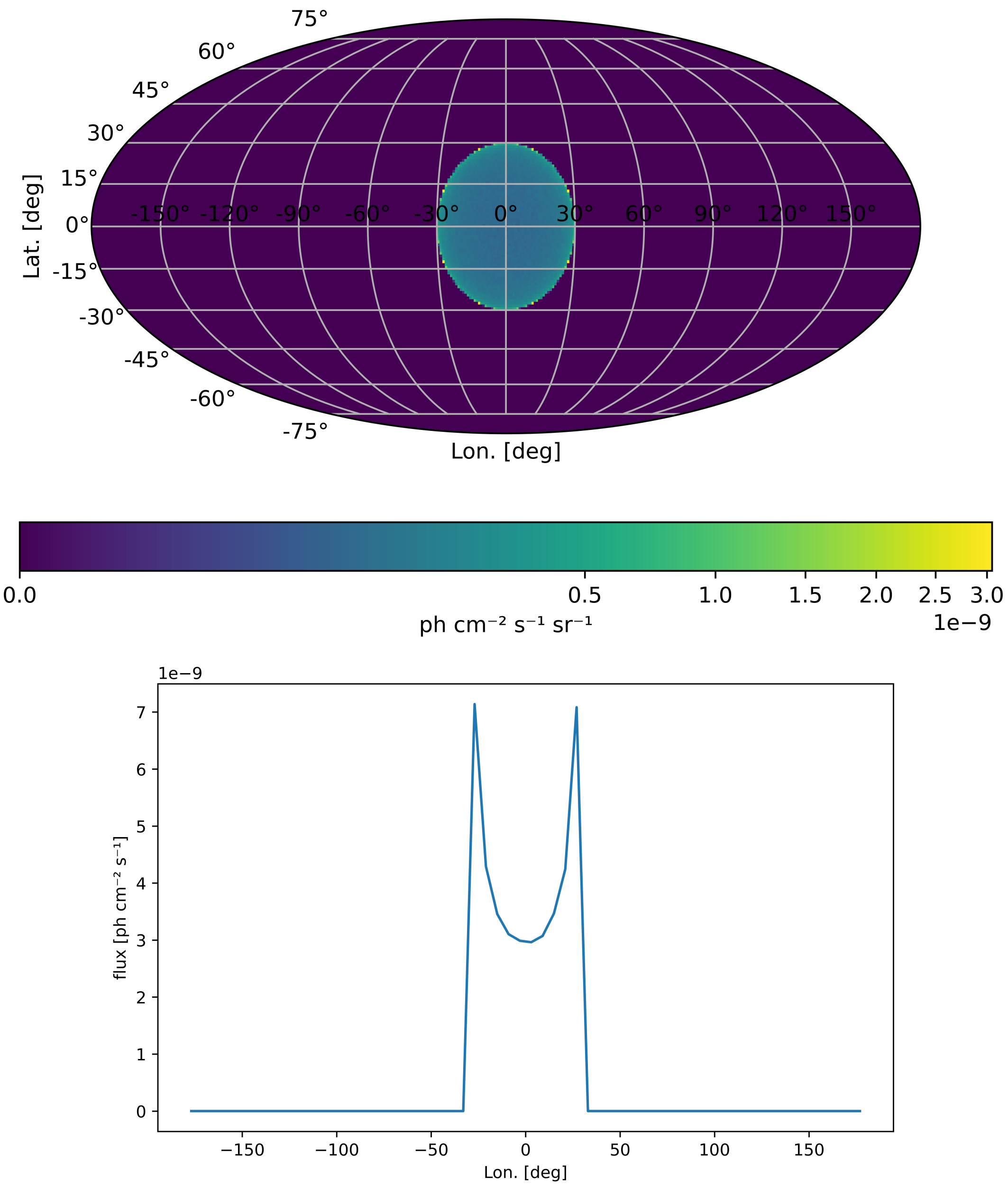

Fig. 32: Top: Sphere with a radius of 500 pc simulated annihilation flux for the position: [x=1000, y=0, z=0].
Bottom: Cross-cut for Lat = 0 °

In Fig. 32 the flux map of a sphere with radius 500 pc at a distance of 1000 pc is shown. A higher flux is observed at the edge (cross-cut of Fig. 32), since here one “looks through” the entire range of annihilations. The corresponding total flux is $4.3 \cdot 10^{-7}\,\mathrm{ph\,cm^{-2}\,s^{-1}}$. Additionally, we estimated flux maps for different positions, which is shown in Fig. 33. The total annihilation flux of the superbubble in the top is $2.9 \cdot 10^{-7}\,\mathrm{ph\,cm^{-2}\,s^{-1}}$ at a distance of 1118 pc. The bottom one at a distance of 1225 pc provides a flux of $2.0 \cdot 10^{-7}\,\mathrm{ph\,cm^{-2}\,s^{-1}}$. We can see that the flux decreases for higher values of the distance d which we expected.

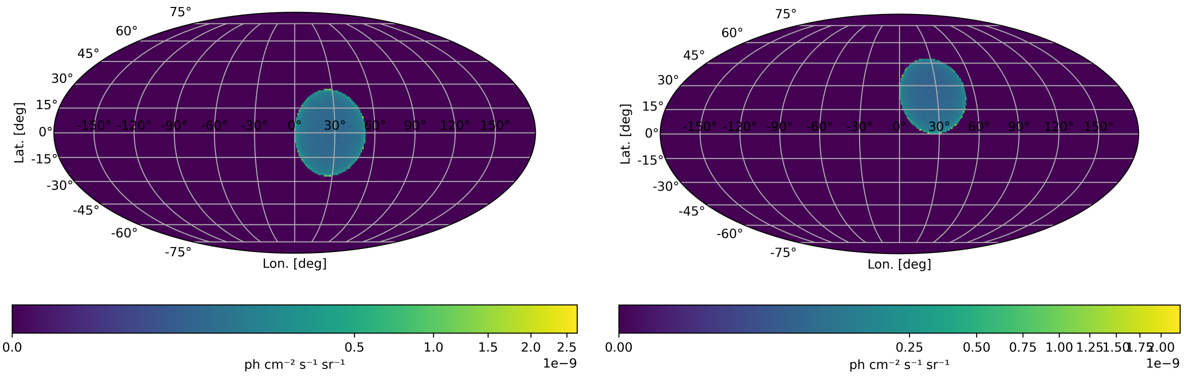

Fig. 33: Top: Sphere with a radius of 500 pc simulated annihilation flux for the position: [x=1000, y=500, z=0].
Bottom: Same sphere simulated annihilation flux for the position: [x=1000, y=500, z=500].

6 Simulations for the Compton Spectrometer and Imager Satellite Mission

In this chapter we will use the previously described setup to perform particle-by-particle Monte-Carlo simulations with GEANT4-based MEGAlib (GEANT4: [Allison et al., 2006]; MEGAlib: [Zoglauer et al., 2006]). The simulations are computationally intense with the entire satellite bus. Therefore, we use a smaller version of COSI-SMEX for testing purposes called COSERL (see Sec. 6.1). The environment in which the simulations take place is the software package `COSItools`[3]. We want to determine whether positron annihilation can be measured with the help of the telescope, or what observation time is necessary for this. The Galactic background of the 511 keV line is simulated as well as a reference.

6.1 COSI telescope geometry

COSI (=COmpton Spectrometer and Imager) is NASA's latest small explorer (SMEX) mission and will launch in 2027. As a Compton telescope it will measure in the soft gamma-ray regime (0.2-5.0 MeV). It has a field of view of 25 % of the sky. The telescope provides an angular resolution of 3.2° FWHM and a line sensitivity of $7.9 \cdot 10^{-6}\,\mathrm{ph\,cm^{-2}\,s^{-1}}$ (3σ narrow line sensitivity in two years of survey observations) for 511 keV [Tomsick and COSI Collaboration, 2022]. Therefore, COSI will improve the sensitivity in this energy band, compared to COMPTEL and INTEGRAL/SPI (Fig. 34).
As a Compton telescope, COSI uses events from Compton scatterings in the detectors. These events give us information on the photon energy and allow us to narrow down the position of the source to a circle at the sky using the scattering angle for each event (Fig. 35). For further events the intersection of these circles reveal the position of the source.
To simulate the whole COSI-SMEX satellite bus is computationally very expensive. For this reason we, use a very simplified mass model, called COSERL (Fig. 36). The advantage of this is a greatly reduced computing time. However, it should be noted that we have to

[3] https://github.com/zoglauer/COSIpy

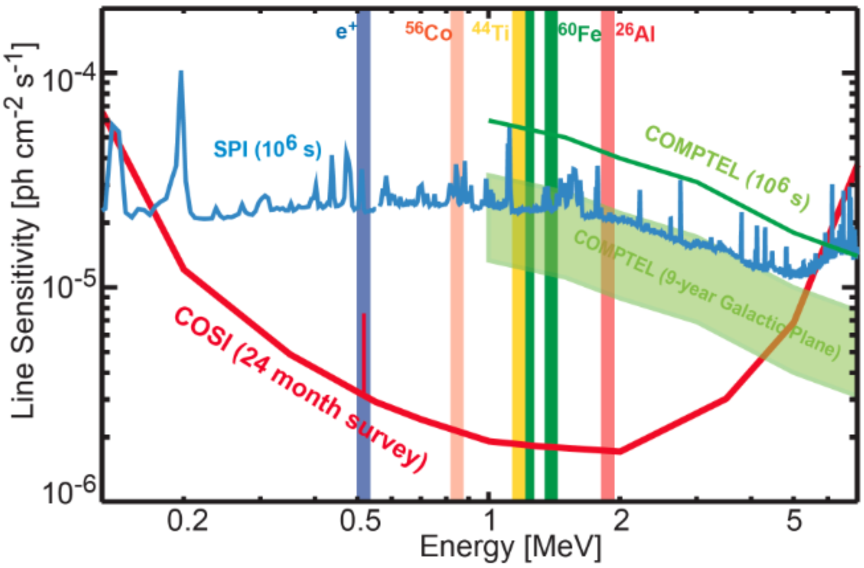

Fig. 34: The COSI narrow line sensitivity for point sources (3σ) compared with COMPTEL and INTEGRAL/SPI. Picture taken from [Tomsick and COSI Collaboration, 2022]

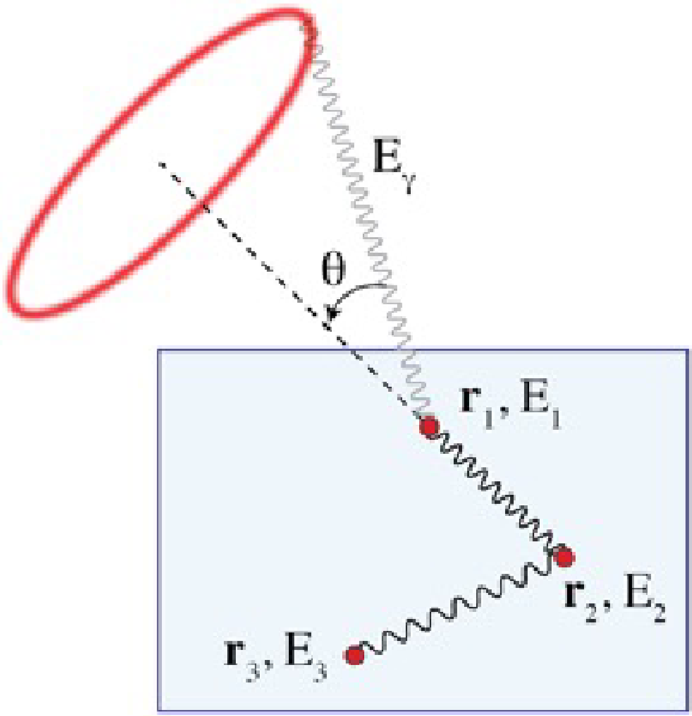

Fig. 35: Schematic representation of a scattering event in a Compton telescope. Picture taken from [Tomsick and COSI Collaboration, 2022]

multiply our flux map by a factor ΔG, since the setup used is less sensitive than the real one.

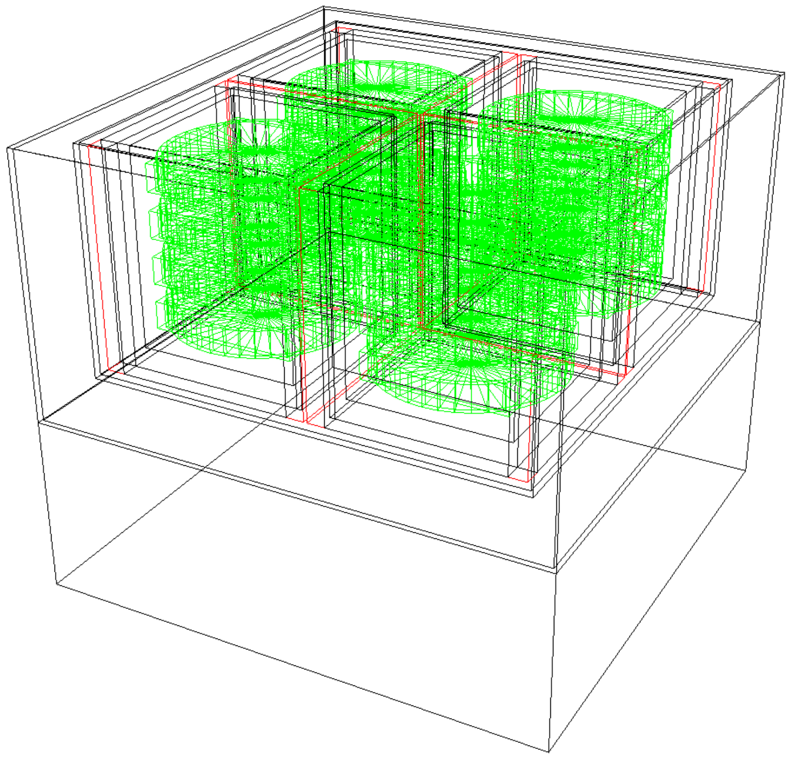

Fig. 36: Used mass model setup for the following simulations.

6.2 Scaling COSERL to COSI-SMEX

We will simulate a flight of the satellite of two years, Therefore, we need to scale the properties of COSERL to COSI-SMEX in order to keep the computational effort a manageable time. First, we need to take into account the time difference of the 25 day exposure and the planned observation time of two years. This results in an additional linear scaling factor (besides ΔG) of $\Delta\mathrm{T} = 2 \cdot 365.25/25 = 29.22$. ΔG is in the order of 10, due to the effective area of COSERL compared to COSI-SMEX [Zoglauer, priv. comm.]. This scaling might also depend on energy and so also differ by another factor of 2 between the mass models. Other factors, like the varying aspect in the COSI-SMEX orbit by $|\pm 22°|$ in each orbit might also have an impact in sensitivity. The angular resolution of COSERL is also worse, compared to COSI-SMEX. In total, we thus obtain a scaling factor of:

$$\mathrm{F} = \Delta\mathrm{G} \cdot \Delta\mathrm{T} \cdot \mathrm{f} = 584.4$$

We use F to multiply our flux maps. This way, we mimic the actually-received counts from the small-scale simulations. This is only a rough estimate of how the SMEX might really perform, but might give us a good order of magnitude estimate on how signicicant the signal received from the Local Bubble could be during a flight for two or more years for the real COSI-SMEX observations.

6.3 Flux Simulations

We will now use `COSIpy` to simulate the observations of both, the Local Bubble and the 511 keV background of the Galaxy. We can draw conclusions of the significance of the Local Bubble compared to the Milky Way by having both components simulated seperately.

We calculated both flux maps for an observation time of two years (multiplied by F=584.4). The total flux of the annihilation map is $1.3 \cdot 10^{-5}\,\mathrm{ph\,cm^{-2}\,s^{-1}}$ while the one of the Galactic background is $2.8 \cdot 10^{-3}\,\mathrm{ph\,cm^{-2}\,s^{-1}}$. The data basis of the Galactic background originates from [Siegert, 2023]. After the simulation of the event reconstruction to show actually measured photons at the detector, the spectra result according to Fig. 37.

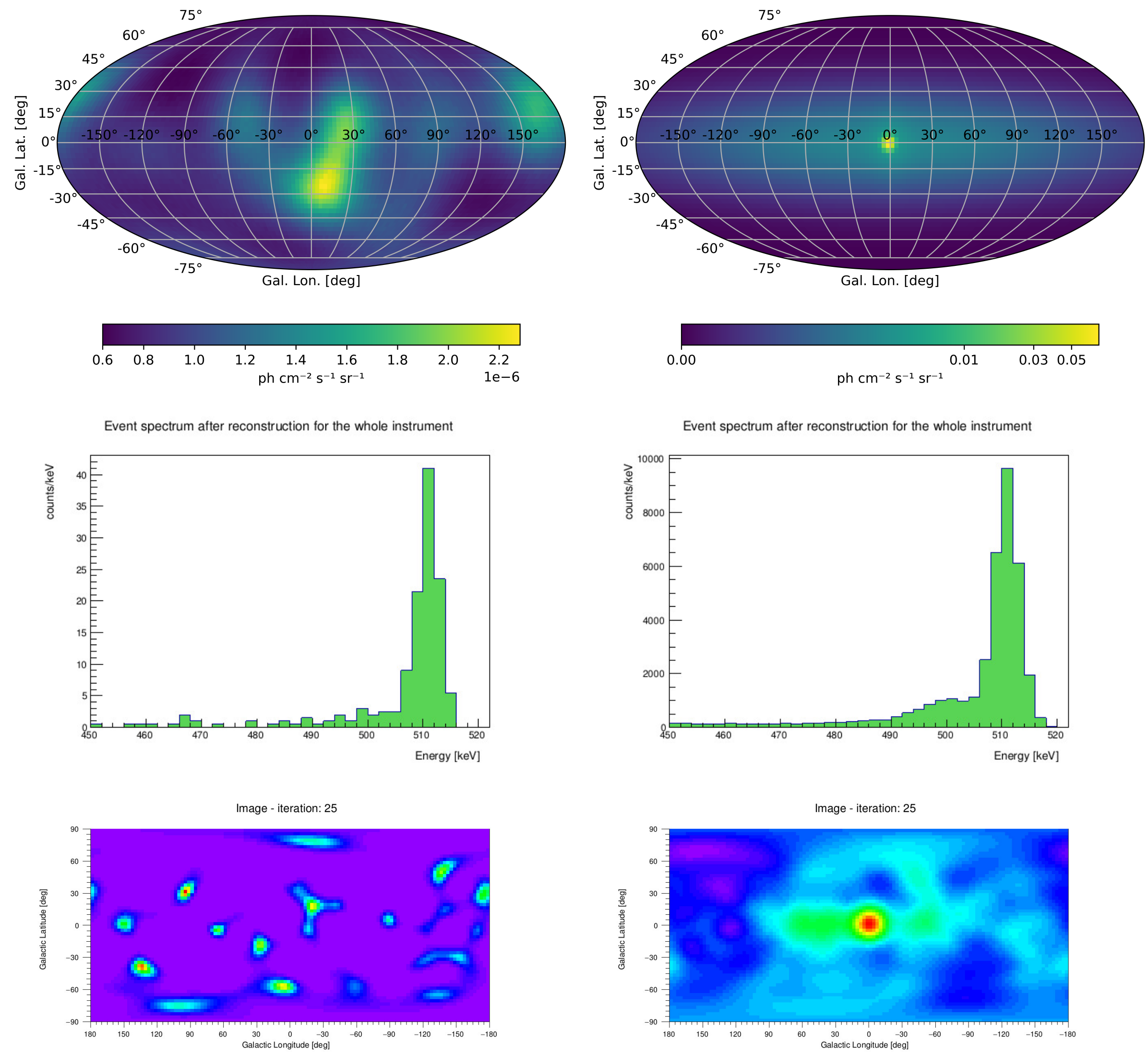

Fig. 37: From top to bottom: flux map used for the simulations, obtained spectra after event reconstruction, image reconstruction map. (Left: Local Bubble flux map; right: Galactic background)

In both spectra, the clear signal of the 511 keV line can be seen, which stands out strongly from the rest of the energy range. The spectrum of the Galaxy appears smoother than the spectrum of the Local Bubble annihilation signal. This can be explained by the significantly higher counts, which logically increase with the flux. In contrast to the Galaxy, the Local Bubble map produces just 1% of the total flux. To illustrate both of the simulated phenomena images of the Galaxy and the Local Bubble map in the 511 keV line were created using the simulated data. Here, the Galactic center stands out (red bump in the center of the image). In contrast to that, the structure of the Local Bubble is not visible at all.

6.4 Significance of the positron annihilation signal

To calculate the significance S of the annihilation signal of the Local Bubble we use the following simplified formula:

$$\mathrm{S} = \frac{\mathrm{C_{LB}}}{\sqrt{\mathrm{C_{BG}} + \mathrm{C_{LB}}}}\,\sigma \tag{25}$$

$\mathrm{C_{LB}}$ are the total counts due to positron annihilation at the edges of the Local Bubble. $\mathrm{C_{BG}}$ is the number of counts due to the 511 keV annihilation signal from the Galactic background. The counts were taken in the energy band of 500-522 keV for both cases.

$$\mathrm{C_{LB}} = 154$$

$$\mathrm{C_{BG}} = 21,989$$

Thus, when inserted into equation 25, the significance $\mathrm{S} = 1.03\,\sigma$.
Such a value for the significance is not very high when considering the observation period of two years. The COSI mission has been authorized by NASA for a period of two years. Based on the calculations of the model derived in this thesis to describe positron annihilation in the Local Bubble, COSI will probably not be able to measure the signal. However, considering the structure of the flux maps, (flux distribution over the sky) the Local Bubble appears very bright at high latitudes, compared to the Galactic background, which would make a detections easier in these areas. Furthermore, the instrumental background at 511 keV has been ignored in these simulations. This signal might worsen the significance estimate.

7 Discussions

7.1 Direct comparison to the 511 keV background map

We simulated the observation of the Local Bubble 511 keV flux in front of the Galactic background. As above-mentioned, the Local Bubble yields $\frac{1.3 \cdot 10^{-5}}{2.8 \cdot 10^{-3}} = 0.0046 = 0.46\%$ of the total flux, compared to the Galaxy. This is in possible reach, considering the COSI-SMEX sensitivity of $7.9 \cdot 10^{-6}\,\mathrm{ph\,cm^{-2}\,s^{-1}}$. But as shown before, this flux is distributed over the whole sky, which results in probably not a detection within the 2 year observation period.

However, we can calculate a difference map of the two fluxes by

$$\mathrm{M_{Diff}} = \frac{\mathrm{M_{LB}} - \mathrm{M_{BG}}}{\mathrm{M_{LB}}} \tag{26}$$

This is shown in Fig. 38.

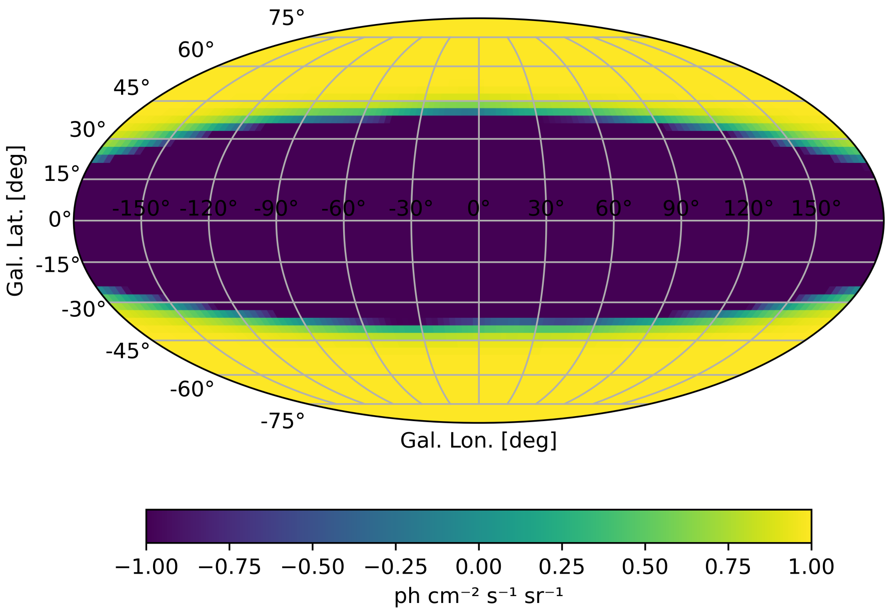

Fig. 38: Difference flux map according to equation 26

.

We can see the bright spots, where the Local Bubble outshines the Galactic background at high latitudes ($|\mathrm{Lat.}| > 45°$). In the Galactic plane on the other hand, the background is much brighter than the Local Bubble and thus makes a detection harder in this region. At the border of the two regions the fluxes (green) are within the same order of magnitude. Summing over these high latitude pixels, gives us a Local Bubble flux of $4.6 \cdot 10^{-6}\,\mathrm{ph\,cm^{-2}\,s^{-1}}$, which means 37% of the total flux lie in the regions where the Local Bubble outshines the Galaxy. COSI has a very large field of view. Furthermore, the COSI-SMEX mission provides a strategy of observing along the ecliptic, which spends more exposure to higher latitudes. This enhances the chances of an observation.

7.2 Comparison to cosmic gamma-ray background lines

We can also compare the Local Bubble flux to the cosmic gamma-ray background. Therefore, we describe the 511 keV gamma-ray line with a Gaussian function. According to [Guessoum et al., 2005], this line has a width of σ=1.1 keV. The Gaussian is given by

$$\mathrm{G} = \frac{\mathrm{F}}{\sqrt{2\,\pi} \cdot \sigma} \cdot \exp\left(\frac{(\mathrm{E} - 511\mathrm{keV})^2}{2 \cdot \sigma^2}\right)$$

with F being the Local Bubble total annihilation flux of $1.3 \cdot 10^{-5}\,\mathrm{ph\,cm^{-2}\,s^{-1}}$. Using this method, we have now obtained a spectrum dN/dE and can compare the maximum at 511 keV with values of the cosmic gamma-ray background. Fig. 39 shows the cosmic background radiation spectrum from microwave to gamma ray energies. It also shows the contribution from of different objects in the galaxy. We see at 511 keV, the whole flux is produced by Seyfert galaxies.

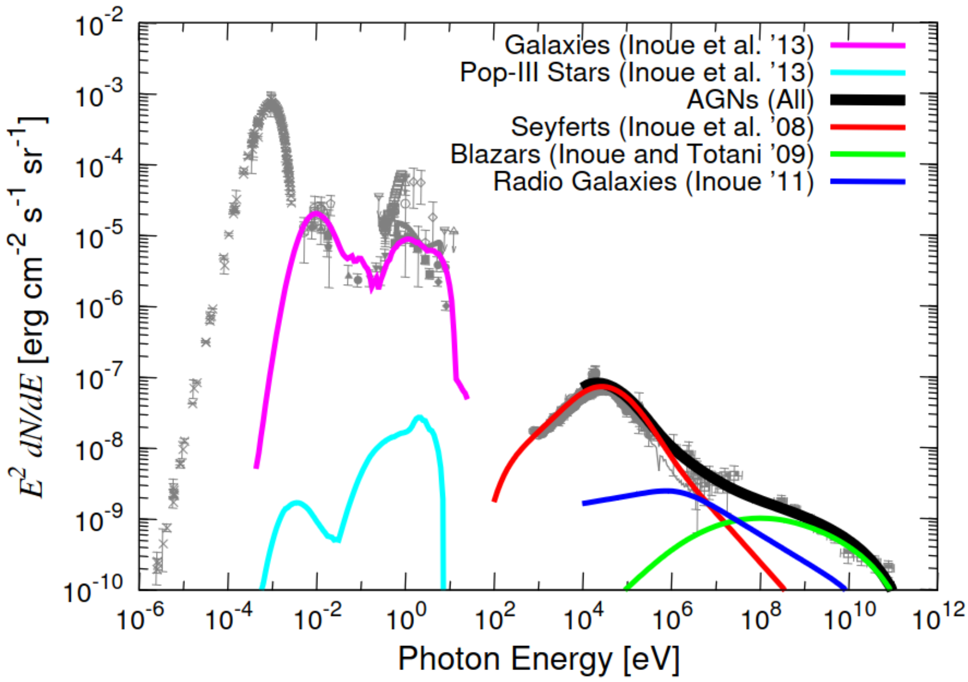

Fig. 39: The cosmic background radiation spectrum from microwave to gamma-ray energies [Inoue, 2014].

The flux value of the gamma-ray background at 511 keV is $1.5 \cdot 10^{-8}\,\mathrm{erg\,cm^{-2}\,s^{-1}\,sr^{-1}}$. Our Gaussian gives us a flux of $1.6 \cdot 10^{-10}\,\mathrm{erg\,cm^{-2}\,s^{-1}\,sr^{-1}}$ which is about two magnitudes of order smaller than the cosmic gamma-ray background at 511 keV. As a result we get that the Local Bubble annihilation signal is much weaker than the cosmic gamma-ray background, but all the flux is confined in an single line which makes it possible to distinguish.

8 Conclusion

In this thesis, the hypothesis of an isotropic contribution of the 511 keV gamma-ray line from the β^+ decay of ^{26}Al to the Galactic and the cosmic gamma-ray background was investigated. We use the estimate of an ejecta mass of ^{26}Al of $7.5 \cdot 10^{-5}\,\mathrm{M}_\odot$ from a recent and nearby supernova within the Local Bubble to calculate the emissivity of positrons.
We make use of the line of sight integration from the point of an observer at the position of the Solar System in the central region of the Local Bubble looking to the edges given by [Zucker et al., 2022]. We modelled the diffusion of the low-energy positrons with simultaneous annihilation inside the Local Bubble, to derive the positron density profile. This results in a total flux providing an isotropic ($\sim$ 65%) as well as an unisotropic contribution.
The expected 511 keV line flux is between $4.9 \cdot 10^{-6}$ and $1.5 \cdot 10^{-5}\,\mathrm{ph\,cm^{-2}\,s^{-1}}$, taking into account the uncertainties of the ejecta mass, the time passed since the last supernova inside the Local Bubble, the cooling timescale and the annihilation time scale of the positrons.
The sensitivity of current telescopes is not sufficient to measure this flux. The future COSI-SMEX mission might see the Local Bubble shell compared to the Galactic background at higher latitudes. Full-sky simulations for COSI with a simplified mass model showed a detection significance below 3σ for an observation time of two years. However, for high latitudes ($> 45°$) the Local Bubble shows a very bright emission compared to the Galaxy which shows nearly no emission in these areas. With suitable analysis techniques, it might be possible to distinguish the two components.
The narrow 511 keV gamma-ray line shows a contribution of 1% to the cosmic gamma-ray background. However, COSI's large field of view combined with the strategy of observing along the ecliptic which spends more exposure at higher latitudes, might make it possible to disentangle the isotropic gamma-ray line from the AGN continuum and the Galactic plane.

Bibliography

[Allison et al., 2006] Allison, J., Amako, K., Apostolakis, J., Araujo, H., Dubois, P. A., Asai, M., Barrand, G., Capra, R., Chauvie, S., Chytracek, R., Cirrone, G. A. P., Cooperman, G., Cosmo, G., Cuttone, G., Daquino, G. G., Donszelmann, M., Dressel, M., Folger, G., Foppiano, F., Generowicz, J., Grichine, V., Guatelli, S., Gumplinger, P., Heikkinen, A., Hrivnacova, I., Howard, A., Incerti, S., Ivanchenko, V., Johnson, T., Jones, F., Koi, T., Kokoulin, R., Kossov, M., Kurashige, H., Lara, V., Larsson, S., Lei, F., Link, O., Longo, F., Maire, M., Mantero, A., Mascialino, B., McLaren, I., Lorenzo, P. M., Minamimoto, K., Murakami, K., Nieminen, P., Pandola, L., Parlati, S., Peralta, L., Perl, J., Pfeiffer, A., Pia, M. G., Ribon, A., Rodrigues, P., Russo, G., Sadilov, S., Santin, G., Sasaki, T., Smith, D., Starkov, N., Tanaka, S., Tcherniaev, E., Tome, B., Trindade, A., Truscott, P., Urban, L., Verderi, M., Walkden, A., Wellisch, J. P., Williams, D. C., Wright, D., and Yoshida, H. (2006). Geant4 developments and applications. *IEEE Transactions on Nuclear Science*, 53(1):270–278.

[Chaikin et al., 2022] Chaikin, E., Kaurov, A. A., Fields, B. D., and Correa, C. A. (2022). Simulations of ^{60}Fe entrained in ejecta from a near-Earth supernova: effects of observer motion. , 512(1):712–727.

[Diehl et al., 2021] Diehl, R., Lugaro, M., Heger, A., Sieverding, A., Tang, X., Li, K. A., Li, E. T., Doherty, C. L., Krause, M. G. H., Wallner, A., Prantzos, N., Brinkman, H. E., den Hartogh, J. W., Wehmeyer, B., Yagüe López, A., Pleintinger, M. M. M., Banerjee, P., and Wang, W. (2021). The radioactive nuclei ({26}) Al and ({60}) Fe in the Cosmos and in the solar system. , 38:e062.

[Guessoum et al., 2005] Guessoum, N., Jean, P., and Gillard, W. (2005). The lives and deaths of positrons in the interstellar medium. , 436(1):171–185.

[Inoue, 2014] Inoue, Y. (2014). Cosmic gamma-ray background radiation.

[Krause et al., 2014] Krause, M., Diehl, R., Böhringer, H., Freyberg, M., and Lubos, D. (2014). Feedback by massive stars and the emergence of superbubbles. II. X-ray properties. , 566:A94.

[Oberlack et al., 1996] Oberlack, U., Bennett, K., Bloemen, H., Diehl, R., Dupraz, C., Hermsen, W., Knoedlseder, J., Morris, D., Schoenfelder, V., Strong, A., and Winkler, C. (1996). The COMPTEL 1.809MeV all-sky image. , 120:311–314.

[Ohlendorf et al., 2010] Ohlendorf, H., Diehl, R., Lang, M., Martin, P., Voss, R., and Preibisch, T. (2010). 26Al emission from the Scorpius-Centaurus association. In *Nuclei in the Cosmos*, page 146.

[Pelgrims et al., 2020] Pelgrims, V., Ferrière, K., Boulanger, F., Lallement, R., and Montier, L. (2020). Modeling the magnetized Local Bubble from dust data. , 636:A17.

[Pleintinger, 2020] Pleintinger, M. M. M. (2020). *Star Groups and their Nucleosynthesis*. PhD thesis, Technische Universität München.

[Prantzos et al., 2011] Prantzos, N., Boehm, C., Bykov, A. M., Diehl, R., Ferrière, K., Guessoum, N., Jean, P., Knoedlseder, J., Marcowith, A., Moskalenko, I. V., Strong, A., and Weidenspointner, G. (2011). The 511 keV emission from positron annihilation in the Galaxy. *Reviews of Modern Physics*, 83(3):1001–1056.

[Siegert, 2023] Siegert, T. (2023). The Positron Puzzle. , 368(4):27.

[Siegert et al., 2019] Siegert, T., Crocker, R. M., Diehl, R., Krause, M. G. H., Panther, F. H., Pleintinger, M. M. M., and Weinberger, C. (2019). Constraints on positron annihilation kinematics in the inner Galaxy. , 627:A126.

[Siegert et al., 2023] Siegert, T., Pleintinger, M. M. M., Diehl, R., Krause, M. G. H., Greiner, J., and Weinberger, C. (2023). Galactic population synthesis of radioactive nucleosynthesis ejecta. , 672:A54.

[Tomsick and COSI Collaboration, 2022] Tomsick, J. and COSI Collaboration (2022). The Compton Spectrometer and Imager Project for MeV Astronomy. In *37th International Cosmic Ray Conference*, page 652.

[Zoglauer et al., 2006] Zoglauer, A., Andritschke, R., and Schopper, F. (2006). MEGAlib The Medium Energy Gamma-ray Astronomy Library. , 50(7-8):629–632.

[Zucker et al., 2022] Zucker, C., Goodman, A. A., Alves, J., Bialy, S., Foley, M., Speagle, J. S., GroÎ²schedl, J., Finkbeiner, D. P., Burkert, A., Khimey, D., and Swiggum, C. (2022). Star formation near the Sun is driven by expansion of the Local Bubble. , 601(7893):334–337.